A&A 676, A112 (2023)
https://doi.org/10.1051/0004-6361/202346016

Astronomy & Astrophysics
Special issue

Solar Orbiter First Results (Nominal Mission Phase)

Extreme-ultraviolet fine structure and variability associated with coronal rain revealed by Solar Orbiter/EUI HRI_{EUV} and SPICE⋆

P. Antolin[1], A. Dolliou[2], F. Auchère[2], L. P. Chitta[3], S. Parenti[2,4], D. Berghmans[4], R. Aznar Cuadrado[3], K. Barczynski[5,6], S. Gissot[4], L. Harra[5,6], Z. Huang[3], M. Janvier[7,2], E. Kraaikamp[4], D. M. Long[8,19], S. Mandal[3], H. Peter[3], L. Rodriguez[4], U. Schühle[3], P. J. Smith[8], S. K. Solanki[3], K. Stegen[4], L. Teriaca[3], C. Verbeeck[4], M. J. West[9], A. N. Zhukov[4,10], T. Appourchaux[2], G. Aulanier[11,12], E. Buchlin[2], F. Delmotte[13], J. M. Gilles[14], M. Haberreiter[5], J.-P. Halain[14,7], K. Heerlein[3], J.-F. Hochedez[15,16], M. Gyo[5], S. Poedts[17,18], and P. Rochus[14]

(Affiliations can be found after the references)

Received 29 January 2023 / Accepted 25 May 2023

ABSTRACT

Context. Coronal rain is the most dramatic cooling phenomenon of the solar corona. Recent observations in the visible and UV spectrum have shown that coronal rain is a pervasive phenomenon in active regions. Its strong link with coronal heating through the thermal non-equilibrium (TNE) – thermal instability (TI) scenario makes it an essential diagnostic tool for the heating properties. Another puzzling feature of the solar corona in addition to the heating is its filamentary structure and variability, particularly in the extreme UV (EUV).
Aims. We aim to identify observable features of the TNE-TI scenario underlying coronal rain at small and large spatial scales to understand the role it plays in the solar corona.
Methods. We used EUV datasets at an unprecedented spatial resolution of ≈240 km from the High Resolution Imager (HRI) in the EUV (HRI_{EUV}) of the Extreme Ultraviolet Imager (EUI) and SPICE on board Solar Orbiter from the perihelion in March and April 2022.
Results. EUV absorption features produced by coronal rain are detected at scales as small as 260 km. As the rain falls, heating and compression is produced immediately downstream, leading to a small EUV brightening that accompanies the fall and produces a fireball phenomenon in the solar corona. Just prior to impact, a flash-like EUV brightening downstream of the rain, lasting a few minutes, is observed for the fastest events. For the first time, we detect the atmospheric response to the impact of the rain on the chromosphere, and it consists of upward-propagating rebound shocks and flows that partly reheat the loop. The observed widths of the rain clumps are 500 ± 200 km. They exhibit a broad velocity distribution of 10−150 km s^{-1} and peak below 50 km s^{-1}. Coronal strands of similar widths are observed along the same loops. They are co-spatial with cool filamentary structure seen with SPICE, which we interpret as the condensation corona transition region. Prior to the appearance of the rain, sequential loop brightenings are detected in gradually cooler lines from coronal to chromospheric temperatures. This matches the expected cooling. Despite the large rain showers, most cannot be detected in AIA 171 in quadrature, indicating that line-of-sight effects play a major role in the visibility of coronal rain. The AIA 304 and SPICE observations still reveal that only a small fraction of the rain can be captured by HRI_{EUV}.
Conclusions. Coronal rain generates EUV structure and variability over a wide range of scales, from coronal loops to the smallest resolvable scales. This establishes the major role that TNE-TI plays in the observed EUV morphology and variability of the corona.

Key words. Sun: corona – Sun: transition region – Sun: activity – Sun: filaments, prominences – magnetohydrodynamics (MHD) – instabilities

1. Introduction

The solar corona is mysteriously heated to millions of degrees by mechanisms of magnetic energy conversion and transport in plasmas that are currently unclear. Coronal loops, the building blocks of the inner solar corona, constitute the prime target for the investigation of coronal heating because they are visible above the diffuse background. Many of their properties remain a puzzle, for example, their lifetimes (EUV variation) and morphologies (in particular, their sub-structure; Reale 2010; Klimchuk 2015; Viall et al. 2021). For instance, a long-standing puzzle of the corona is the observed filamentary or strand-like structure of loops (as opposed to being diffused) and their high variability, particularly in spectral lines in the upper transition region (TR; Kjeldseth-Moe & Brekke 1998; Ugarte-Urra et al. 2009; Hinode Review Team 2019). The filamentary structure is linked with the loop sub-structure, and the concept of coronal strands is introduced and usually assumed to be part of a larger entity (or coronal loop bundle). This multi-stranded versus monolithic structure has long been debated in the solar community. Its importance stems from its strong link with the fundamental scales on which the heating operates in the solar atmosphere, which is either directly associated with the scales at the granular level, where most of the energy originates (Martínez-Sykora et al. 2018), or is associated indirectly, for example, by modifying how magnetohydrodynamic (MHD) waves propagate and dissipate in inhomogeneous plasmas (Van Doorsselaere et al. 2014, 2020).

Prior to the launch of Solar Orbiter (Müller et al. 2020), Hi-C (first and second flights; Kobayashi et al. 2014; Rachmeler et al. 2019) provided observations with the highest spatial resolution in the EUV, namely in the Fe XII 193 Å line, which forms at ≈1.5 × 10^6 K (first flight), and in the Fe IX 172 Å line, which forms at ≈$10^{5.9}$ K (second flight). These observations

⋆ Movies are available at https://www.aanda.org

indicated coronal strand widths of about a few hundred kilometers (Peter et al. 2013; Brooks et al. 2013; Aschwanden & Peter 2017; Williams et al. 2020). On the other hand, this sub-structure does not appear to be present for all coronal loops and in different temperature regimes, as the above reports show. Sub-structure such as coronal strands may appear during the evolution of the loops, particularly their cooling, and thus may be linked to specific aspects of how the cooling occurs.

Coronal rain is the most dramatic display of cooling in the solar corona. It corresponds to cool (10^3–10^5 K) and dense (10^{10}–10^{13} cm^{-3}) plasma clumps appearing over a timescale of minutes in chromospheric and TR spectral lines in the solar corona that preferentially fall towards the solar surface along coronal loops (Kawaguchi 1970; Leroy 1972; Foukal 1978; Habbal et al. 1985; Wiik et al. 1996; Schrijver 2001; De Groof et al. 2004, 2005). Coronal rain is closely related to prominences (Vial & Engvold 2015), but high-resolution observations over the past decade with Hinode (Kosugi et al. 2007; Antolin & Shibata 2010; Hinode Review Team 2019), the Swedish 1-m Solar Telescope (SST; Scharmer et al. 2003; Antolin & Rouppe van der Voort 2012), the *Goode* Solar Telescope (GST; Goode et al. 2003; Ahn et al. 2014; Jing et al. 2016), the Solar Dynamics Observatory (SDO; Pesnell et al. 2012; Vashalomidze et al. 2015), and the Interface Region Imaging Spectrograph (IRIS; De Pontieu et al. 2014, 2021; Antolin et al. 2015; Schad 2017) have shown that coronal rain presents unique features in terms of its morphology and kinematics. At the smallest scales, coronal rain appears to be composed of clumps that also seem to constitute the coolest and densest part. The widths (in the direction transverse to the flow) can be as small as 120 km (Jing et al. 2016), but are generally a few hundred kilometers in Hα (Antolin & Rouppe van der Voort 2012) to ≈500–600 km in TR lines (Antolin et al. 2015), with little variation other than that expected by spatial resolution. On the other hand, they can be greatly extended longitudinally (along the flow), with lengths of about an order of magnitude or more. Recently, Şahin et al. (2023) studied large-scale coronal rain over an active region (AR) with IRIS in chromospheric and TR lines, finding little variation in its morphological and dynamical properties over several hours and across the AR. The widths of the observed coronal rain strands appear to be very similar to those of the coronal strands observed by Hi-C, described above, which may either directly reflect a fundamental heating scale (Jing et al. 2016; Antolin & Froment 2022) or be associated with the cooling, as explained below.

One of the most interesting aspects of coronal rain is that the clumps occur in tandem across a relatively large cross-section across the magnetic field (a few megameters in width). This synchronicity and shared trajectory of clumps has led to the concept of a rain shower, that is, a larger structure composed of coronal rain clumps (Antolin & Rouppe van der Voort 2012). Şahin & Antolin (2022) have shown that rain showers match cooling coronal loops observed in the EUV well, thereby helping us to identify these in the large superposition (leading to line-of-sight confusion) of the optically thin solar corona (referred to by Malanushenko et al. 2022, as 'coronal veil').

There are currently three different types of coronal rain. The most commonly observed type is known as quiescent and preferentially occurs in AR coronal loops. This type does not require any specific magnetic topology (other than a loop-forming bipolar structure). The second type is linked to solar flares and is known as flare-driven coronal rain. It corresponds to the cool chromospheric loops (sometimes known as Hα loops) that appear at the end of the gradual phase. The last type is known as prominence-coronal rain hybrids and involves a complex magnetic field with a null-point topology at the top of loop arcades. A review of each can be found in Antolin & Froment (2022). This work concerns the first type, that is, the quiescent coronal rain of ARs. This type is studied most actively, probably because of its strong link with coronal heating.

Numerical work since the 1990s has shown that complex magnetic topologies such as magnetic dips are not necessary for the generation of cool and dense prominence-like structures in loops (Antiochos & Klimchuk 1991; Antiochos et al. 1999; Karpen et al. 2001). Although we do not know the agents of coronal heating exactly (e.g. MHD waves or stress-induced magnetic reconnection), the generated spatial and temporal distribution of the magnetic energy along loops has unique consequences for the evolution of coronal loops, specifically, for how they cool. When the heating is strongly stratified (also known as 'footpoint concentrated'), even when it is constant over time, the loop is often unable to reach thermal equilibrium and enters a state of thermal non-equilibrium (TNE). Its thermodynamic evolution undergoes cycles of heating and cooling, generally referred as TNE cycles, which are also known as evaporation-condensation cycles (Kuin & Martens 1982; Mok et al. 1990; Reale et al. 1996; Müller et al. 2003; Mendoza-Briceño et al. 2005; Susino et al. 2010; Luna et al. 2012). This is true as long as the repetition frequency of the stratified heating events is faster than the radiative cooling time of the loop (Johnston et al. 2019). Klimchuk & Luna (2019) have quantified some of the requirements needed for TNE and found that a volumetric heating ratio between apex and footpoint below 0.3 and a heating asymmetry between both footpoints under 3 ensures TNE.

In a nutshell, with a strongly stratified heating, the loop apex relies on thermal conduction for its heating. However, this spatial distribution leads to an essentially flat temperature profile along the loop length or even a temperature dip at the apex, thus making conduction inefficient. Furthermore, the footpoint heating is very efficient at injecting material upwards (through chromospheric ablation or evaporation), making the loop overdense relative to the RTV scaling law (Rosner et al. 1978). The apex becomes thermally imbalanced, which results in runaway or catastrophic cooling because plasmas are more efficient in radiating their energy away at lower temperatures (in the TR – corona temperature range). While the heating can be very rapid (with the loop essentially empty) and therefore very hard to observe, the cooling progresses over a timescale of tens of minutes to hours, depending on the loop conditions. These long cooling times can lead to very long loop lifetimes (Lionello et al. 2016). The loop eventually evacuates, and the cycle restarts if the heating conditions do not change, hence leading to cycles of heating and cooling. During the initial stages of the cooling and when the cooling time is long enough relative to the cadence of the observations, the loop is expected to sequentially appear in cooler coronal passbands with specific non-zero time lags (Kamio et al. 2011; Viall & Klimchuk 2012; Viall et al. 2021). The cyclic pattern can lead to highly periodic EUV intensity pulsations on the order of hours, as were recently detected with EIT (Auchère et al. 2014) and the Atmospheric Imaging Assembly (AIA; Lemen et al. 2012; Froment et al. 2015), indicating a heating function that is stable over days (and up to a week). At the end of the cooling part of the TNE cycle, accelerated cooling is observed and coronal rain appears, which can therefore also occur periodically (Auchère et al. 2018; Froment et al. 2020). This acceleration in the cooling rate and also the spatial and temporal character of coronal rain have been interpreted as a product of thermal instability (TI), but a debate exists in the

community (Klimchuk 2019; Antolin 2020). The essential role that TI may play in the observed coronal rain phenomena (and probably in the long-period intensity pulsations as well) has led to the cycles being known as TNE-TI cycles (Antolin & Froment 2022).

Thermal instability is a fundamental MHD process (Parker 1953; Field 1965; Waters & Proga 2019; Claes & Keppens 2019). In addition to coronal rain, it has been invoked to explain phenomena from short laboratory scales (Lipschultz 1987; Stacey 1996) to very large intracluster medium scales (White & Rees 1978; Cavagnolo et al. 2008; Sharma 2013). In the context of the solar corona, thermal instability is less straightforward to apply because the corona is very dynamic and is out of hydrostatic equilibrium (Aschwanden et al. 2001). Nonetheless, various analytic studies have argued that given the long timescales of TNE cycles, TI theory still holds, given the local and short timescale characteristics of its occurrence (Claes & Keppens 2021). Antolin & Rouppe van der Voort (2012) and Antolin et al. (2015) have argued that TI may act as a synchronising mechanism for catastrophic cooling to occur simultaneously across a loop in TNE, thereby providing an explanation for rain showers (see also Froment et al. 2020; Antolin 2020). Şahin & Antolin (2022) have used this link to unlock a way for estimating the TNE volume over an AR. By calculating the number of rain showers and their properties, they have estimated that at least 50% of the AR is subject to TNE.

2.5D radiative MHD simulations by Antolin et al. (2022) have shown that the TI-driven catastrophic cooling leads to the formation of cool and dense cores at the head of the rain emitting in chromospheric lines. These cores are surrounded by thin but strongly emitting shells in TR lines that elongate in the wake of the rain, in what is known as the condensation corona transition region (CCTR). These structures are seen clearly in the Si IV 1402 line observed by IRIS (forming at $\approx 10^{4.8}$ K) and in the Fe XII 171 line observed by AIA 171 (forming at $\approx 10^{5.8}$ K). They might therefore explain the filamentary or stranded morphology and dynamic nature of the corona seen in these lines (Ugarte-Urra et al. 2009), as well as the common widths between coronal rain strands and coronal EUV substructure. High-resolution observations in the EUV are needed to confirm this hypothesis. Furthermore, Antolin et al. (2022) have shown that TI produces a local enhancement of the magnetic field strength that is due to the gas-pressure loss during TI and frozen-in conditions. Through the compression ahead of the rain (downstream) as it falls, a strong UV and EUV enhancement is obtained over the last few megameters prior to impact with the chromosphere. Furthermore, a strong rebound shock and upward flow is obtained from the impact, which propagate at different speeds (corresponding to the tube speed and flow). These features have remained elusive in observations until now.

Solar Orbiter was launched in early 2020 on a highly elliptical orbit around the Sun. By now, it has concluded two science close perihelia in its nominal mission phase, where the distance to the Sun was less than 0.32 au. In this work, we analyse data from one of the two High Resolution Imagers (HRI) of the Extreme Ultraviolet Imager (EUI) telescopes on board Solar Orbiter (Rochus et al. 2020). The data correspond to the first close perihelion, which occurred between March and April 2022 (Berghmans et al. 2023). The $\mathrm{HRI_{EUV}}$ is an EUV imaging instrument in the 174 Å passband. This passband is dominated by the Fe IX (at 171.1 Å) and Fe X (at 174.5 Å and 177.2 Å) emission forming at $\approx 10^6$ K (Chen et al. 2021). The importance of the high resolution achieved by this instrument was already evident in $\mathrm{HRI_{EUV}}$ data from May 2020, when the spacecraft was at 0.556 au. Small EUV brightenings were revealed at spatial and temporal resolutions that could be barely detected by SDO/AIA observations (known as 'campfires'; Berghmans et al. 2021).

EUI also includes a high-resolution imager $\mathrm{HRI_{Lya}}$, whose bandpass is centred at 121.6 nm and is dominated by the Lyman-α line of hydrogen. We do not use $\mathrm{HRI_{Lya}}$ in this work because of the degradation issues of the telescope during the perihelion approach (see Berghmans et al. 2023, for details).

In this work, we analyse $\mathrm{HRI_{EUV}}$ data and identify several coronal rain events at the unprecedented spatial resolution of ≈240 km in the EUV. This resolution allows us to clearly identify the EUV variability and morphology associated with coronal rain. The paper is organised as follows. The $\mathrm{HRI_{EUV}}$ observations are presented in Sect. 2. The methods are presented in Sect. 3. Results can be found in Sect. 4, and the discussion and conclusions are given in Sect. 5.

2. Observations

The observations analysed in this work belong to the first perihelion passage of Solar Orbiter in March and April 2022. Specifically, we analyse two datasets of $\mathrm{HRI_{EUV}}$ at 174 Å, one of NOAA 12974 on 2022 March 30, and the other of ARs NOAA 12975 and 12796 on 2022 April 1st, both on-disk (Mampaey et al. 2022). At this time, Solar Orbiter was near quadrature with Earth (with separation angles between Solar Orbiter and the Sun-Earth line of 91.88° and 102.02° for March 30 and April 1st, respectively).

On March 30 and April 1st, Solar Orbiter was at 0.33 au and 0.34 au, respectively. With an $\mathrm{HRI_{EUV}}$ plate scale of 0.492″, the spatial resolution of these observations is estimated to be close to the Nyquist limit of $2 \times 0.492''$ (Berghmans et al. 2023), corresponding approximately to 237 km and 247 km. HRI images have 2048×2048 pixels, leading to a $17' \times 17'$ field of view (FOV). The full FOV for each date can be seen in Fig. 1. The observations on March 30 and April 1st are part of the R_BOTH_HRES_HCAD_Nanoflares and R_SMALL_MRES_MCAD_AR-Long-Term SOOPs (Zouganelis et al. 2020), respectively, which operated the $\mathrm{HRI_{EUV}}$ camera at a cadence of 3 s over a duration of 45 min (UT 00:03–00:48) on March 30, and at a cadence of 10 s over a duration of ≈75 min (UT 09:19–10:34) on April 1st.

EUI is equipped with software-controlled onboard calibration electronics to correct the images pixel-wise for offset and flat field before compression. The images are then prepped with the euiprep routine to level 2, which reduces the jitter and pointing error. However, significant jitter still remains that needs to be removed. To this end, we applied a cross-correlation technique to align the images as described in Chitta et al. (2022).

For better visualisation of the fine structure in the $\mathrm{HRI_{EUV}}$ images, we applied the wavelet-optimised whitening (WOW) enhancement technique described in Auchère et al. (2023). This method works by equalising the variance at all scales and locations in the image, thereby reducing the large-scale gradients and conversely enhancing the small-scale structures.

We also checked $\mathrm{HRI_{Lya}}$ for the presence of rain in the Lyman-α line. However, none could be detected, probably due to the problem affecting the resolution of the instrument, as discussed in Berghmans et al. (2023).

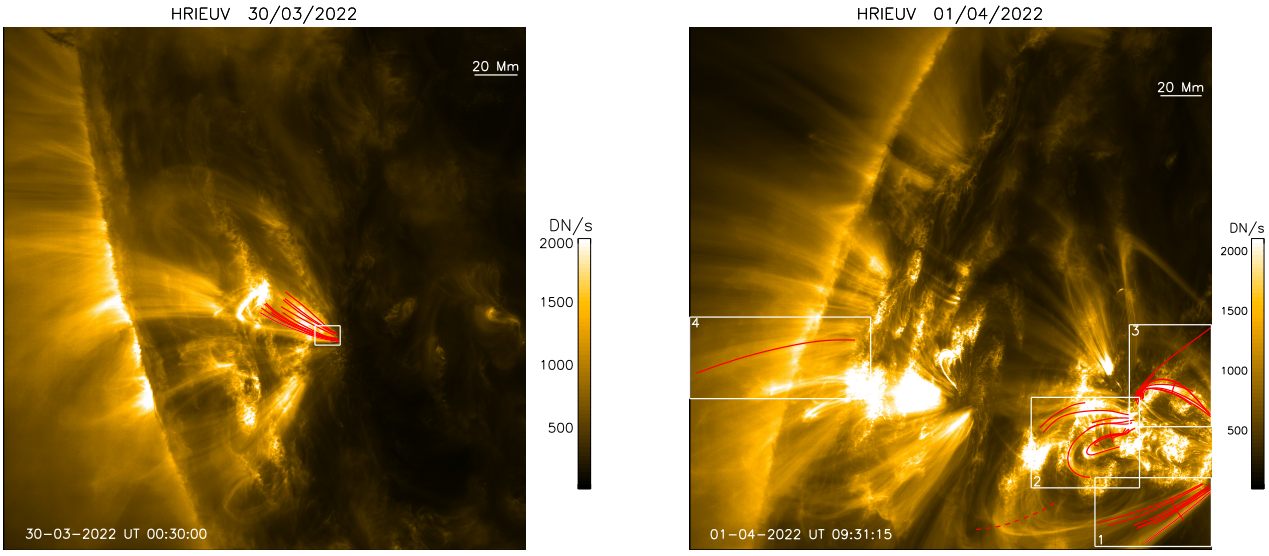

Fig. 1. Full FOV of HRI_{EUV} for the 2022 March 30 (left) and April 1st (right) datasets. The inner white rectangles show the sub-FOVs that are shown in later figures. The solid red curves denote the trajectories of some of the observed coronal rain clumps.

Solar Orbiter also carries the Spectral Imaging of the Coronal Environement (SPICE; SPICE Consortium 2020) as part of the remote-sensing payload. For March 30, the SPICE data we analysed (data release 3.0[1]) are the 96-step raster starting at 00:00:32 UTC with a FOV of 384″ × 914″. It has a duration of 16 min 24 s and an exposure time of 10 s. The selected slit is 4″ wide, and the data spatial pixel size is 1.098″ along the slit. The temperature coverage of the spectral windows was from the chromosphere to the corona through the observation of the following spectral lines: H I Lyβ 1025.72 Å ($\log T_e$ = 4.0 K), C III 977.03 Å ($\log T_e$ = 4.8 K), S V 786.47 Å ($\log T_e$ = 5.2 K), O IV 787.72 Å ($\log T_e$ = 5.2 K), O VI 1031.93 Å ($\log T_e$ = 5.5 K), Ne VIII 770.42 Å ($\log T_e$ = 5.8 K), and Mg IX 706.02 Å ($\log T_e$ = 6.0 K). For April 1st, we analysed five 160-step rasters that used the 4″ slit, each producing a FOV of 640″×911″. They run from 09:15:36 to 10:15:37 UTC. The raster duration is 14 min with an exposure time of 5 s. The spectral windows of April 1st covered similar lines as the March 30 raster, with the exception of the S V and O IV lines. These two lines were replaced by N IV 765.15 Å ($\log T_e$ = 5.2 K). For both datasets, we used L2 data, which are original data corrected for dark current, flat field, and geometrical distortion. An additional step in the data processing was the application of the radiometric calibration.

The pointing information in the SPICE L2 headers is not accurate and the SPICE rasters need to be co-aligned with the HRI_{EUV} sequence. We started by binning the HRI_{EUV} images to the same pixel size as SPICE. We then built a HRI_{EUV} synthetic raster (SR) by selecting from the HRI_{EUV} time sequence the image closest in time to each SPICE exposure making the raster. For each SPICE exposure, the SPICE pixel positions along the slit make an irregular grid in helioprojective coordinates. The HRI_{EUV} image closest in time to this exposure is reprojected onto this grid. We then made SPICE images in Ne VIII intensity by spectrally summing over the 32-pixel window. The Ne VIII and HRI_{EUV} images are comparable in terms of plasma temperature coverage. Finally, the SPICE images were co-aligned with the HRI_{EUV} synthetic raster using a cross-correlation technique. The SPICE FOV for March 30 and April 1st in the Ne VIII line co-aligned with HRI_{EUV} can be seen in Fig. 2.

[1] https://doi.org/10.48326/idoc.medoc.spice.3.0

In addition to EUI images, we also briefly analysed images from the Atmospheric Imaging Assembly (AIA; Lemen et al. 2012) on board the Solar Dynamics Observatory (SDO; Pesnell et al. 2012) to locate, if possible, the coronal rain events observed with HRI_{EUV}. The AIA data correspond to level 2 data, processed through the standard SolarSoft packages. Since strict AIA-EUI co-alignment at a pixel scale is not needed for our purpose (we do not need to identify specific rain trajectories across different viewpoints), we relied on co-alignment using header information through the JHelioviewer software (Müller et al. 2009), which is sufficient to identify the large-scale structure common to both FOVs (e.g. loops, rain showers, or prominences).

3. Method

Coronal rain clumps and showers can be seen with a sharp eye without an image-enhancement technique such as WOW, but they certainly become more discernible in the processed images. To analyse the morphology and dynamics of several of these events, we started by tracking several rain clumps manually in the image sequences with the help of the crisp spectral explorer (CRISPEX), a widget-based tool programmed in the Interactive Data Language (IDL), which enables the easy browsing of the data, the determination of loop paths, extraction, and further analysis of space-time diagrams (Vissers & Rouppe van der Voort 2012).

The projected velocities in the plane of the sky (POS) were determined by calculating slopes in the resulting rain clump tracks in the time-distance diagrams obtained from CRISPEX. These tracks define the (x, y, t) positions of the rain. The errors incurred in this process depend on the length of the tracks in the time-distance diagrams. By varying the spatial and temporal end points of the tracks slightly, it is possible to estimate the errors in each calculation. The availability of AIA in quadrature would allow us to estimate the total speed of a rain event through 3D stereoscopy. However, this is beyond the scope of the present manuscript.

No rain is detected in the time-distance diagrams (through dark or bright propagating features) without prior check with the image sequences. This is necessary because several effects (e.g.

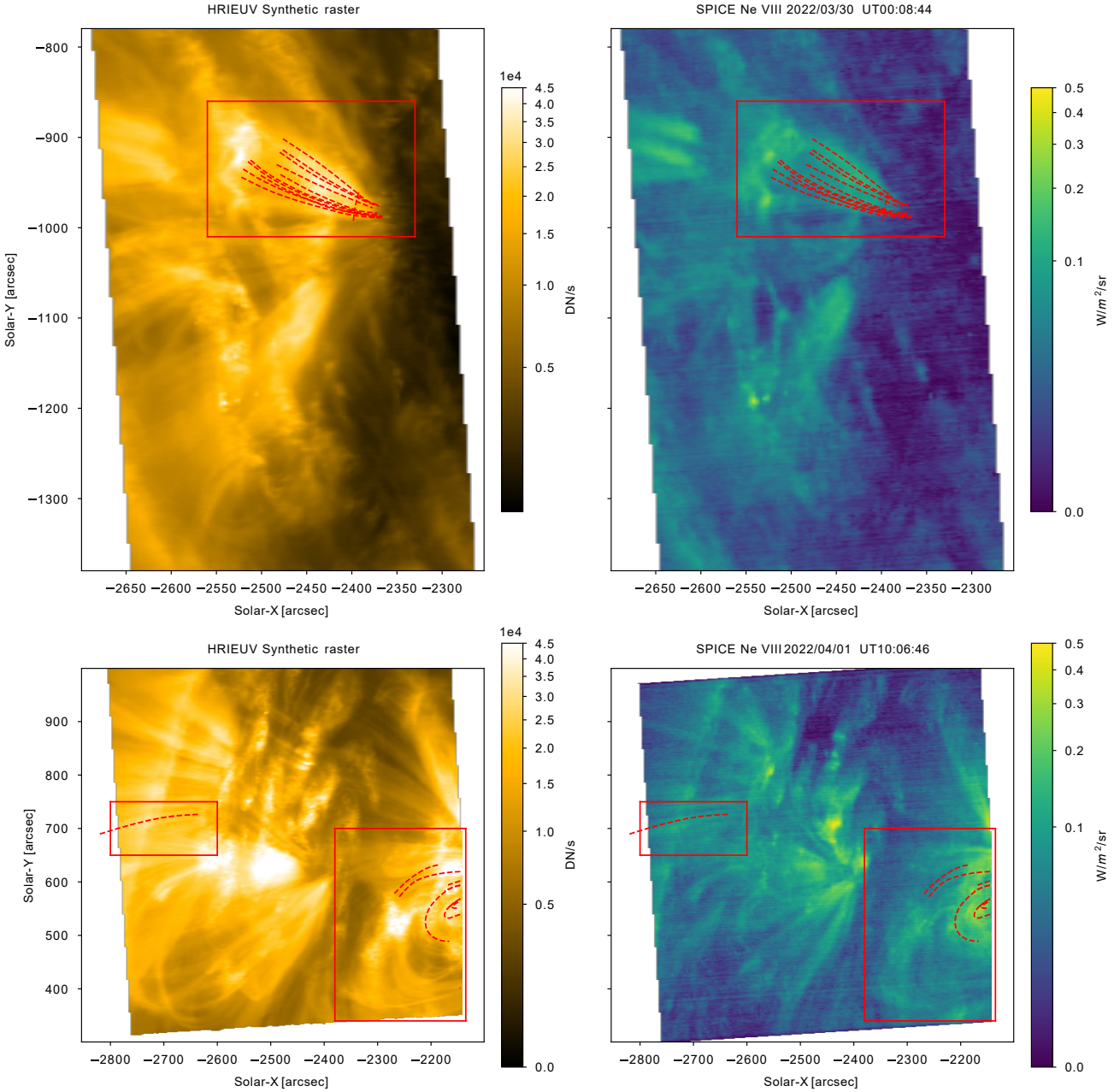

Fig. 2. Co-aligned $\mathrm{HRI_{EUV}}$ (left) and SPICE (right) full FOV for March 30 (top) and April 1st (bottom). The SPICE images correspond to 96- and 160-step rasters for March 30 and April 1st, respectively, and show the total intensity over the Ne VIII line. The corresponding $\mathrm{HRI_{EUV}}$ images are synthetic rasters that match the time and space distribution of the data acquisition with SPICE. A spatial binning has been applied to $\mathrm{HRI_{EUV}}$ to match the plate scale of SPICE. The red rectangles correspond to ROIs in each FOV. Overlaid rain paths in red are identified with $\mathrm{HRI_{EUV}}$. The ROI on March 30 is shown in Fig. 4. The ROIs on April 1st to the west and east are shown in Figs. 12 and 17, respectively. See the text for further details.

lateral motions of loops) can produce apparent dark or bright propagating features in time-distance diagrams.

We were primarily interested in the observed widths in the rain. For this purpose, we applied the same semi-automatic routine as in previous work (for more details, see Antolin et al. 2015). For a given clump path and a given track in the time-distance diagram corresponding to this path, the routine takes a cut perpendicular to the trajectory at every (x, y, t) location defined by the track and fits a single Gaussian over the interpolated profile. The full width at half maximum (FWHM) is then taken as the width of the clump at that location. Several checks were performed to reduce errors in the fitting. We first calculated the average intensity profile of a feature for the time range in which it was seen (as defined by a slope in the time-distance diagram) and required a difference of at least $100\,\mathrm{DN\,s^{-1}}$ between its intensity (which can be in emission or absorption) and the background (which was also calculated over the same path, but at times without rain, immediately before or after the rain episode). We then required the contrast between the average intensity of the feature and the background to be at least 10%. Lastly, we also required that the Gaussian fit of the rain feature was good enough. The latter was ensured by

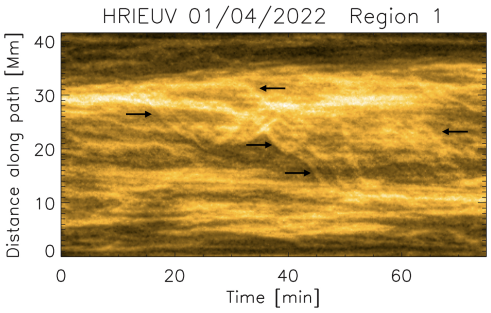

Fig. 3. Time-distance diagram along the dashed white curve in Fig. 1 (right panel) for the April 1st HRI_{EUV} observation. The distance 0 corresponds to the western end of the curve. The curve crosses a loop bundle at the apex, which is seen to undergo a large-scale reconfiguration (radially inward, corresponding to shrinkage), as pointed out by the arrows. This time-distance diagram is made from images that have been processed with the wavelet-optimised whitening enhancement technique of Auchère et al. (2023).

requiring that the σ error resulting from the fit was below 0.4 and that the total of the residuals from the fit was low, that is, $\sum |I_{x,y}(x_\perp, y_\perp, t) - f(x_\perp, y_\perp, t)| < 0.75$, where $(x_\perp, y_\perp)$ denotes the transverse cut to the path at point (x, y), I is the intensity along this cut, and f denotes the Gaussian fit to I. Visual inspection of the fittings indicates that these values ensure an accurate calculation of the rain width while avoiding artefacts due to cosmic rays or other features. The width of a clump corresponds to the average over all measurements performed for the track in the time-distance diagram corresponding to that clump. A measure of the error in the width calculation is given by the standard deviation over all the measurements for a given track.

4. Results

4.1. Coronal loop bundles

We analysed several coronal rain events observed with HRI_{EUV}. On March 30, the event occurred in a coronal loop bundle belonging to AR NOAA 12974 in the southern hemisphere, which is on-disk, but near the limb, as seen in Fig. 1 (left panel). The rain is seen to fall onto the leading polarity, onto a region with an abundance of dark jet-like structures fanning outwards. No sunspot is seen in the vicinity, suggesting that this corresponds to a decaying AR. Several rain clumps were followed, whose trajectories can be seen in the figure.

On April 1st, HRI_{EUV} observed a wide region of activity composed of two ARs, NOAA 12975 and 12976, in the northern hemisphere, also not far from the limb, as seen in Fig. 1 (right panel). Coronal rain is seen much more pervasively than in the other HRI_{EUV} observation. In particular, we analysed four different regions that are labelled in the panel. Several coronal rain events can be seen, as indicated in the figure.

Region 1 focuses on the west footpoint of a very large coronal loop bundle that is seen to undergo a wide-scale reconfiguration. Some of this reconfiguration is also associated with a bundle of loops that is rooted closer to the lower right corner of box 2 in the right panel of Fig. 1. To see this more clearly, we made a transverse cut at the apex of the loop bundle, as shown by the dashed curve in the right panel, and we plot the time-distance diagram in Fig. 3 (distance 0 in the diagram denotes the western end of the dashed curve, as seen in Fig. 1). In the diagram, we indicate several instances of large-scale motions of individual coronal strands directed radially inwards with arrows. These

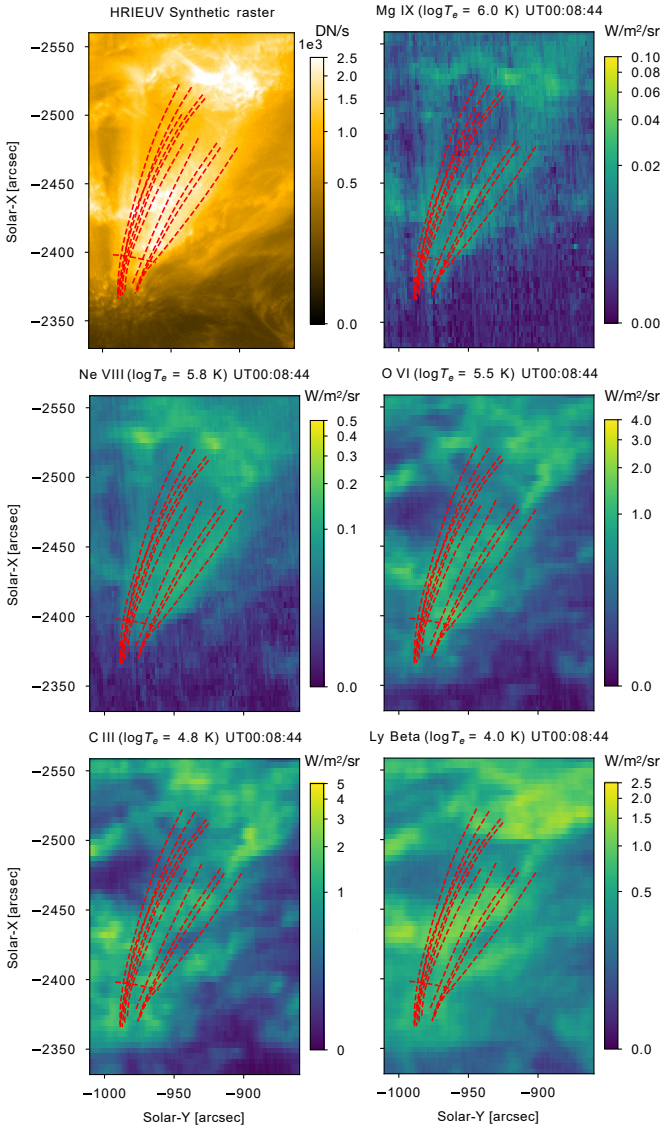

Fig. 4. SPICE multi-wavelength view of the loop bundle with rain seen on March 30. The FOV corresponds to the red rectangle shown in Fig. 2 (top), and the overlaid red curves mostly denote the rain paths seen with HRI_{EUV} (see Fig. 5). The HRI_{EUV} panel corresponds to a synthetic raster matching the time of the SPICE raster (see text for details), but preserving the HRI_{EUV} spatial resolution. Each SPICE panel shows the total intensity over a spectral line indicated in the subtitle, together with its temperature of maximum formation.

instances suggest a shrinkage. This process is also accompanied by large-amplitude transverse oscillations that can also be identified in the figure. At the same time, large amounts of coronal rain are observed to fall along the leg captured in region 1.

Region 2 on April 1st focuses on a region with a different polarity compared to region 1, where the other footpoint of the loop bundle appears to be rooted. Region 2 shows stronger activity (pores, moss, light walls, and jets) and a more complex magnetic topology, as discussed in the accompanying paper (Berghmans et al. 2023). Between regions 1 and 2, a highly twisted filament is seen, whose eruption was observed by EUI and SPICE on the following day, and is discussed in Berghmans et al. (2023).

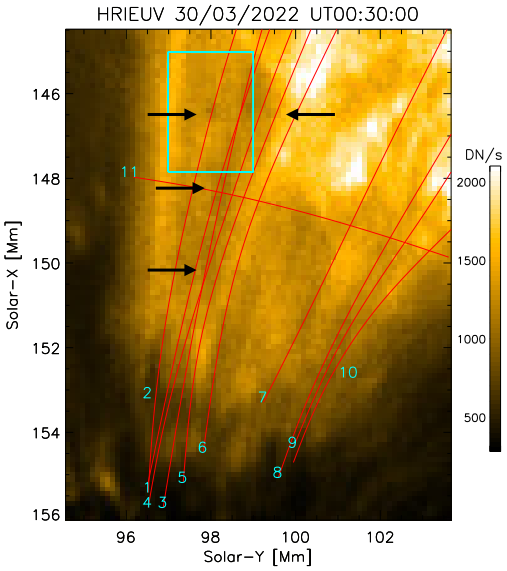

Fig. 5. Close-up of the footpoint of the loop bundle where coronal rain is seen on March 30. The FOV corresponds to the white rectangle shown in Fig. 1 (left), rotated by 90° so that the loop is orientated with the height of the page. The vertically oriented and labelled red curves denote several rain clump trajectories. The black arrows point to some of the clumps. The image corresponds to the average over three consecutive frames. The cyan rectangle in the figure corresponds to the FOV shown in Fig. 7. Path 11 is a transverse cut across the loop bundle. The online animation runs from UT 00:23 to UT 00:37 and shows several coronal rain clumps in absorption that fall towards the chromosphere (dark structure at the bottom). The EUV varies strongly in this event. The images from which the movie is composed are processed with the wavelet-optimised whitening enhancement technique of Auchère et al. (2023). The movie first runs without and then with the rain paths overlaid.

Region 3 on April 1st is located north-west of the AR. A different bundle of loops is seen, with footpoints close to those in region 2. This is therefore also in a high-activity region.

Region 4 on April 1st is located on the east limb. It captures part of a long loop that is rooted in the trailing AR (NOAA 12976).

4.2. March 30 loop bundle as seen with SPICE

Several of the loop bundles seen in $\mathrm{HRI_{EUV}}$ can also be seen in SPICE in the Ne VIII line, as expected from the similar formation temperature. In particular, the loop bundle where rain is observed with $\mathrm{HRI_{EUV}}$ can be seen with SPICE. In Fig. 4 we show a close-up of the loop bundle, which includes the FOV shown in Fig. 5. The raster through this region occurred at UT 00:08:44, which is roughly 20−25 min prior to the main rain shower. The loop can be seen in the Mg IX coronal line and in the upper TR lines (Ne VIII and O VI), suggesting that it is in a state of cooling. However, emission in the lower temperature lines seems to be dominated by the background, and we cannot detect any clear chromospheric emission from coronal rain. This could also be due to timing because the main rain shower occurs after the raster.

SPICE also executed high-cadence three-step rasters at various times during the $\mathrm{HRI_{EUV}}$ observing window, including the rain shower time. However, the slit crosses higher up along the loop at $X \approx -2500''$ (barely crossing a few of the longer rain paths), which coincides with a strong background emission. We could not find any clear rain signatures in these fast rasters.

4.3. Two-pixel-wide coronal rain clumps in absorption, and downstream compression and heating

In Fig. 5 we show several coronal rain paths identified for the event of March 30. The coronal rain clumps can be seen in the figure and in the corresponding animation as dark features, produced by EUV absorption from neutral hydrogen and neutral and singly ionised helium (Anzer & Heinzel 2005). In Fig. 6 (top panel) we show several snapshots separated by 15 s each, where large and small absorption features can be seen to fall.

For better visualisation of the fine-scale structure, we show in Fig. 7 a sub-FOV of only 2 Mm × 3 Mm centred on a dark absorption feature produced by a clump (white rectangle in Fig. 5). We note that it is barely 2 pixels wide (i.e. ≈240 km) and is therefore the image with the highest resolution of a rain clump in EUV absorption to date. Another interesting feature is the bright region downstream of the clump. The animation shows that this bright feature is always beneath the dark absorption feature from the clump. Similar features can be seen for other clumps, some of which appear only moments prior to impact in the chromosphere. We interpret this feature as compression and heating produced by falling individual clumps.

To show the EUV variation produced by the rain more clearly, we plot in Fig. 8 the time-distance diagrams corresponding to paths 2 and 3, shown in Fig. 5. The dark tracks in this figure correspond to the EUV absorption produced by the rain as it falls. The observed slopes indicate average speeds of 70−80 km s^{-1}. Immediately below the first dark track, a parallel bright slanted track can be seen, corresponding to the compression and heating downstream of the rain clump. We note that several such bright tracks can be seen, but are all very short, with lengths shorter than 1 Mm (vertical axis in the time-distance diagram).

Although we did not calculate the lengths of the clumps in this work accurately, a rough estimate is given by the size of the dark tracks (vertical distance) in the time-distance diagrams of Fig. 8, which can be seen to have 1−5 Mm lengths.

4.4. Rebound shock and flow

Figure 6 (lower panel) shows another interesting feature of the event from March 30 that is also seen in the animation of Fig. 5. Following the impact of the rain shower on the chromosphere, a bright upward-propagating feature can be seen. We interpret this as a rebound shock and flow produced by the rain impact. To the best of our knowledge, this is the first time that a feature like this is observed, although it has been predicted by every numerical simulation of coronal rain (e.g. Müller et al. 2003; Fang et al. 2015). This feature can also be seen in each time-distance diagram of Fig. 8 as a bright upward slope just after the end of the rain shower. The slope indicates speeds between 50−130 km s^{-1}. The lower end of this velocity range matches the expected value for upward flows, while the upper end matches the tube speed for a plasma temperature of $10^{5.8}$ K, which is close to the temperature at the peak of the Fe X 174 Å formation. This is also supported by numerical simulations (Antolin et al. 2022).

4.5. Extent of the rain shower

To examine the extent of the rain shower, we plot in Fig. 9 the time-distance diagrams corresponding to all the paths shown in Fig. 5. Several clump tracks are shown by dashed lines. The main rain shower occurs in the time range t = 20−30 min. Although it can best be seen in paths 2 to 5, traces of it are visible across

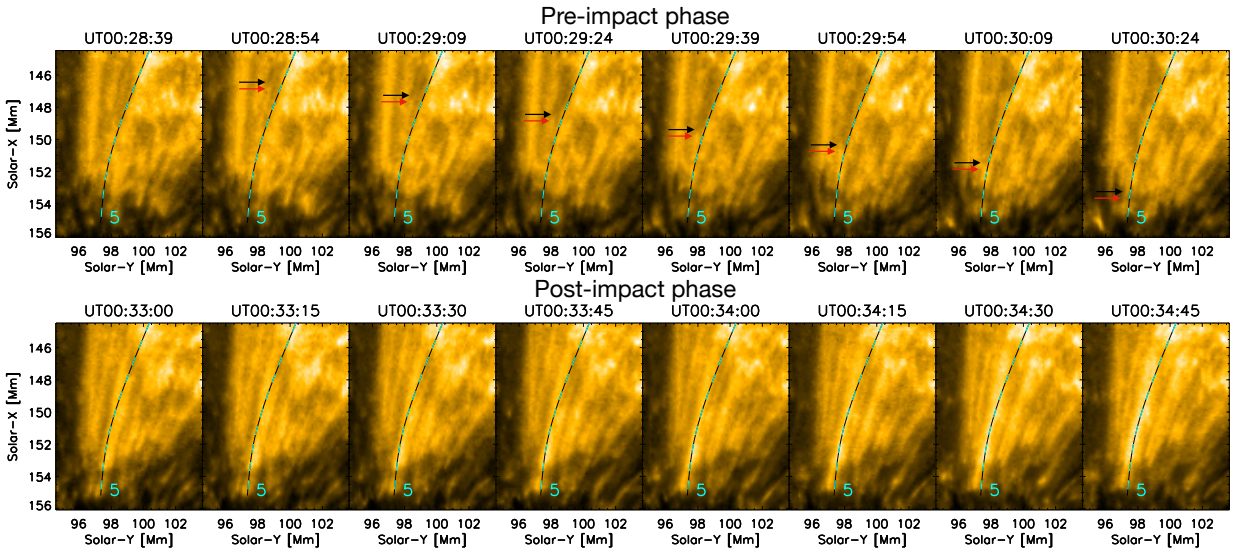

Fig. 6. Sequence of eight snapshots separated by 15 s showing the pre- (top) and post-impact (bottom) phases of a coronal rain shower from the event of March 30. The black arrows in the top panels show the head of a rain clump as it falls (note the bright tip indicated by red arrows, followed by a dark elongated structure). For reference, path 5 is shown in the figure with a dashed cyan-black curve (same labelling as in Fig. 5). The lower panel shows a bright upward-propagating feature corresponding to the combination of the rebound shock and flow produced by the impact of the rain shower. These images have been processed with the wavelet-optimised whitening enhancement technique of Auchère et al. (2023).

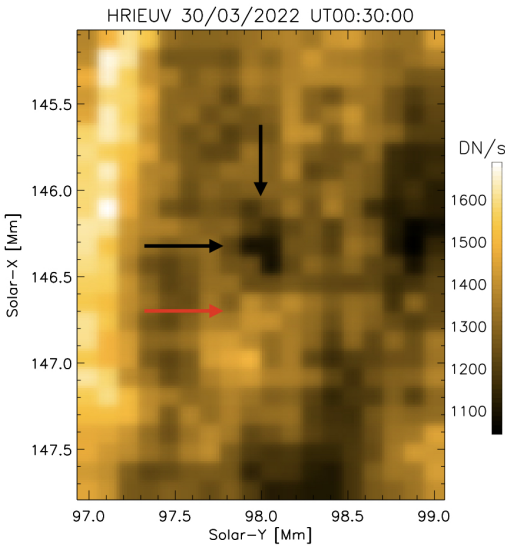

Fig. 7. Close-up of the sub-FOV indicated by the white rectangle in Fig. 5. The dark feature indicated by the arrows corresponds to the EUV absorption produced by a rain clump. We interpret the bright feature below (downstream of) the rain clump indicated by the red arrow as compression and heating produced by the rain clump as it falls.

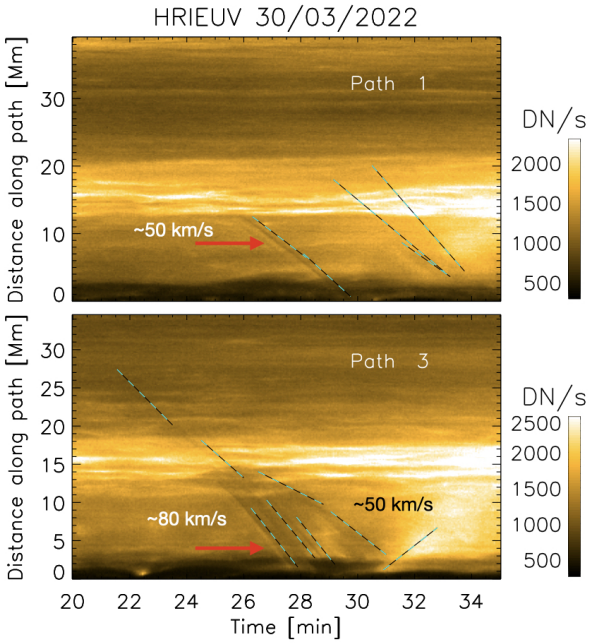

Fig. 8. Time-distance diagrams along paths 1 and 3 indicated in Fig. 5. The distance increases with height along the paths. The dark tracks traced by the dashed cyan-black lines correspond to EUV absorption from falling rain clumps. The dashed lines are offset by a fraction of a minute so that the rain features appear more clearly. An estimate of the projected velocity is given for the closest slope to each value. We note the bright tracks that are indicated by the red arrows immediately beneath the first dark tracks in each diagram. We interpret this feature as compression and heating from the clump. We interpret the upward bright and diffuse slope at the end of the time sequence ($t \approx 30$–32 min) in path 3 as a combination of a rebound shock and flow produced by the rain impact on the chromosphere.

all the paths. This indicates that the extent of the rain shower across the loop bundle is at least 15 Mm in the POS and possibly larger given the observed expansion of the loop bundle seen in Fig. 1 (left panel). This is supported by the SPICE observations in Fig. 4, which show cool TR emission over a width larger than that set by the rain clumps detected by $\mathrm{HRI_{EUV}}$. Along the loop, the clumps can be tracked for up to 25 Mm. We note that many clumps are clearly visible in the last 10 Mm alone, suggesting that the catastrophic cooling is non-uniform. Accelerated cooling rates down to chromospheric temperatures appear to be more confined to the transverse direction. This effect may also be due to the line of sight, as shown in Sect. 4.13.

Figure 9 also shows that the rebound shock and flow occurs across a wide expanse, but appears to be more concentrated than the rain shower and can only be clearly seen in paths 1–6.

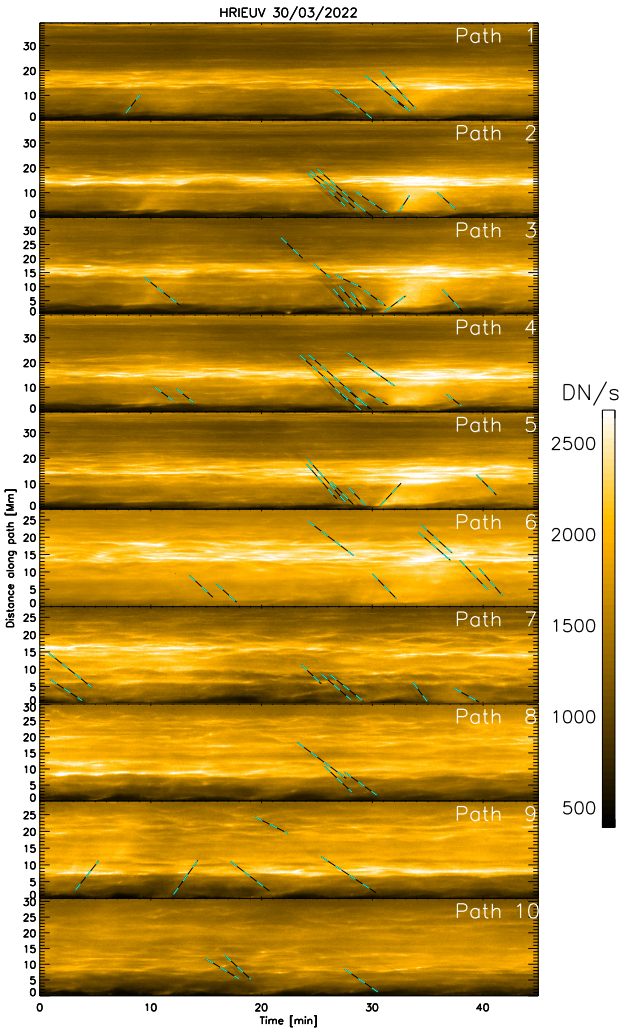

Fig. 9. Time-distance diagrams for all coronal rain paths shown in the left panel of Fig. 1. The dashed cyan-black lines with negative slopes show some of the tracks produced by the rain clumps as they fall. The lines are offset in time by 1 min to show the rain features better. We note the extent of the rain shower across all paths. Upward-propagating features (positive slopes) can also be seen, particularly at the end of the rain shower ($t \approx 30$ min). Zero distance corresponds to the footpoint of the loop (seen in Fig. 5).

4.6. Region 1 on April 1st: A large coronal rain event

We now turn our attention to some of the coronal rain events seen in the April 1st dataset (see Fig. 1, right panel). In Fig. 10 we show the close-up of the footpoint of the large coronal loop bundle undergoing a global change (similar to shrinkage), denoted region 1 in Fig. 1 (right). We follow several rain clumps and plot the corresponding time-distance diagrams in Fig. B.1. A main shower event is seen in the time range $t = 40-70$ min, in particular, along paths 2–4, but signatures of another rain shower are also seen at the beginning ($t < 20$ min), in particular, along paths 6–7. In this case, a combination of neighbouring dark and bright paths are also visible. Although not as clear as for the March 30 event, some of the bright tracks may correspond to the downstream compression and heating, especially those that immediately precede the absorption feature. We note that some of these tracks only appear bright, for example the last track of path 6. Furthermore, upward-propagating features can also be observed, some of which seem to appear just after the rain impact. The

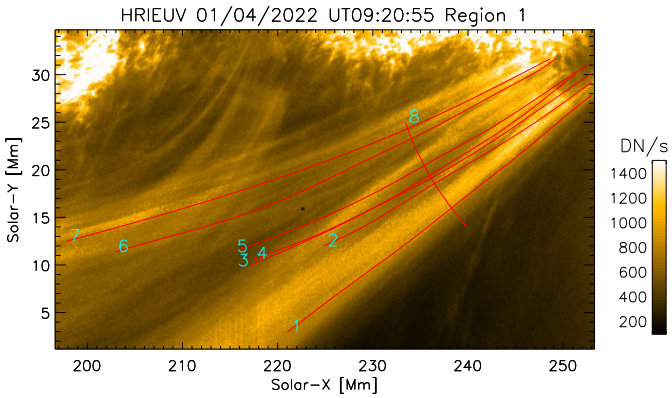

Fig. 10. Close-up of the footpoint of a large coronal loop bundle observed on 2022 April 1st by HRI_{EUV}. The FOV corresponds to that of region 1 indicated by the white rectangle in the right panel of Fig. 1. Except for path 8 (which crosses the loop bundle), the red paths denote several rain paths. An animation of this figure is available online, whose images have been processed with the wavelet-optimised whitening enhancement technique of Auchère et al. (2023). It runs from UT 09:19 to UT 10:34 and shows several rain clumps falling towards the chromosphere. The movie first runs without and then with the rain paths overlaid.

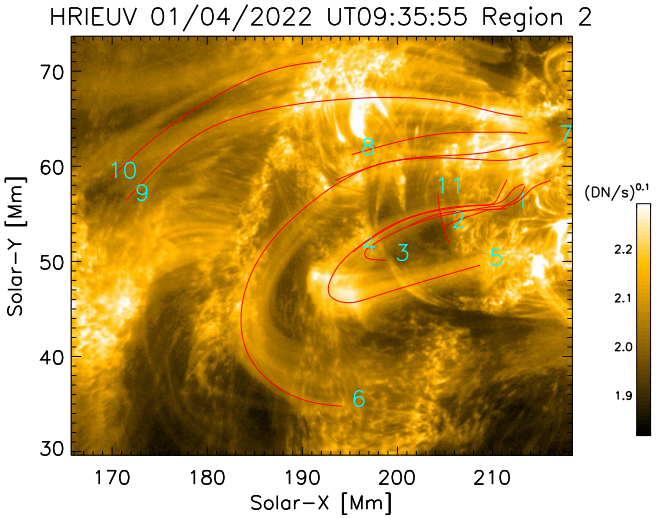

Fig. 11. FOV corresponding to region 2, shown in Fig. 1 (right panel). The red curves correspond to paths of some of the observed coronal rain clumps. We note that the intensities are scaled with a power of 0.1 to show a wider range of variations. An animation of this figure is available online, whose images have been processed with the wavelet-optimised whitening enhancement technique of Auchère et al. (2023). It runs from UT 09:19 to UT 10:34 and shows several rain clumps falling towards the chromosphere. The movie first runs without and then with the rain paths overlaid.

observed morphology and speeds are similar to those seen for the March 30 event, all of which are calculated and presented in Sect. 4.11.

The rain shower seen in region 1 appears to be far wider in extent than that of March 30. As seen in Fig. 10, the transverse length across which the clumps are seen is at least 20 Mm, but is certainly greater given the observed expansion. Furthermore, the clumps can be followed for longer lengths along the loop, and some are tracked for over 40 Mm. This suggests catastrophic cooling down to chromospheric temperatures over a larger coronal volume, which is supported by SPICE observations.

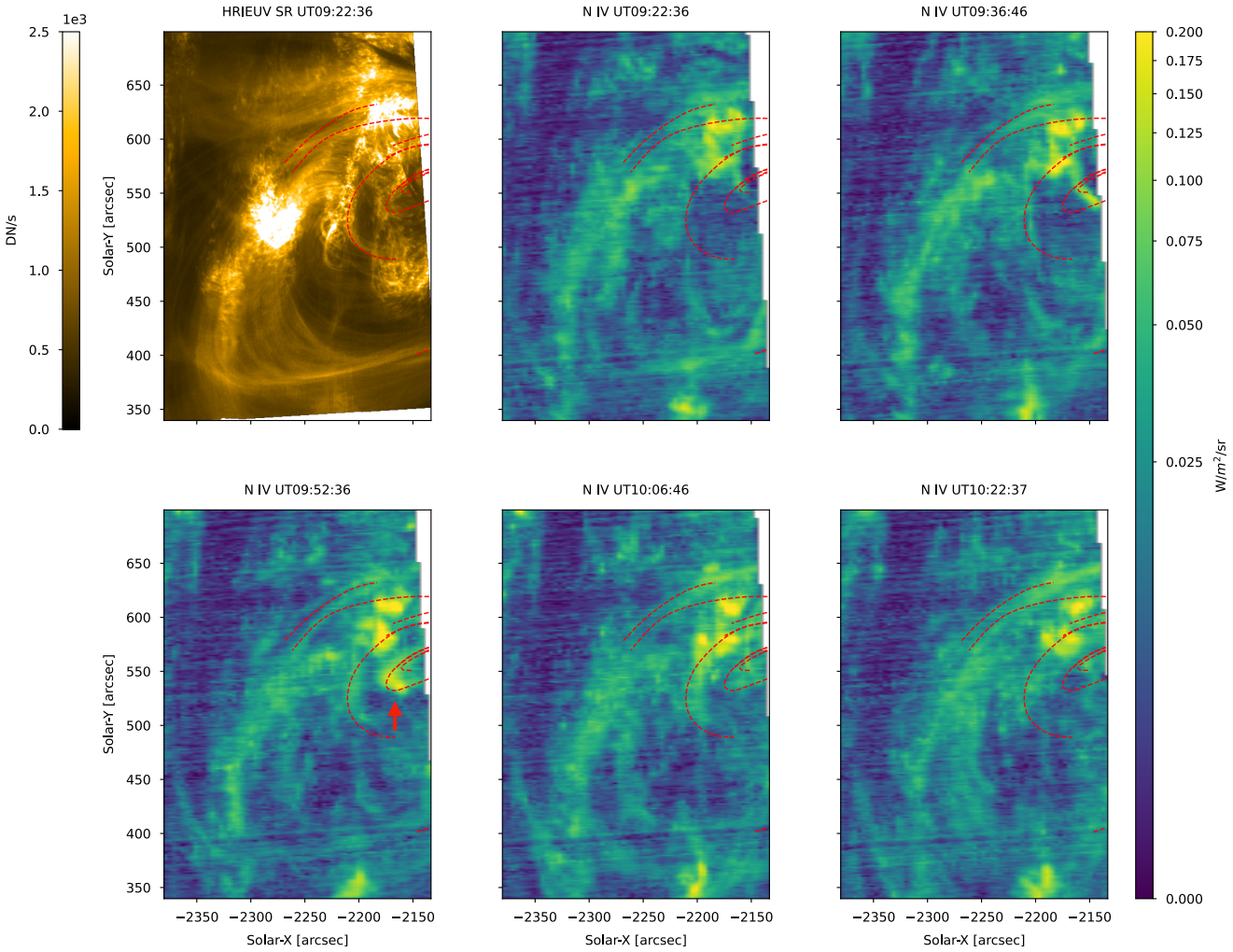

Fig. 12. SPICE rasters in the N IV line ($\log T = 5.2$ K) over a region that overlaps with regions 1 and 2 on April 1st. The FOV corresponds to the red rectangle to the east shown in Fig. 2 (bottom), and the overlaid red curves denote some of the rain paths seen with $\mathrm{HRI_{EUV}}$ (see Figs. 10 and 11). The $\mathrm{HRI_{EUV}}$ panel corresponds to a synthetic raster matching the time of the first SPICE raster (see text for details), but preserving the $\mathrm{HRI_{EUV}}$ spatial resolution. The SPICE panels show the total intensity integrated over the N IV spectral line for each raster (the time is shown in the subtitle). The brightening indicated by the red arrow in the UT 09:52:36 panel corresponds to cooling through the passband.

4.7. Region 2 of April 1st: Null-point topology at the footpoint

Region 2 on April 1st shows several coronal rain events belonging to different regions in the AR. In Fig. 11 we show the FOV corresponding to region 2, as shown in the full FOV of Fig. 1 (right panel), with several rain clump paths overlaid. The corresponding time-distance diagrams for these paths are shown in Fig. B.2.

The most interesting rain shower is tracked by paths 1−5 in these figures. First, a loop bundle appears, in which the intensity throughout the loop increases in a uniform manner (but in particular at the apex) around UT 09:30 (about 10 min from the start of the observation). This brightening can be best seen along path 5 (white arrows in Fig. B.2). The intensity uniformly decreases along the loop over the next 10 min, after which the first rain clumps appear. The bulk of the rain is visible after 20 min from the first intensity increase. Following the rain shower impact, the intensity increases strongly at the footpoint, with some signatures of upward-propagating features (red arrow in Fig. B.2). As the rain falls, it is observed to deviate strongly from its path and to spread in different directions, which is reminiscent of the null-point topology structure at the footpoint.

Paths 6−7 and possibly path 8 seem to correspond to another loop bundle that also experiences a uniform and global loop brightening similar to that described above. In this case, the loop bundle brightens at the very start of the observation and disappears after almost 1 h. The rain is seen roughly 50 min after the start of the brightening, but it is much fainter in terms of EUV absorption than for the previous case. This loop is rooted close to a pore, and periodic upward/downward ballistic motion is seen (in particular, for paths 7 and 8), which is characteristic of Type 1 spicules (Beckers 1964) or the EUV counterparts of AR dynamic fibrils (Mandal et al. 2023).

Path 9 (and possibly path 8 as well) may correspond to the other footpoint of the large loop bundle of region 1. However, in contrast to the other footpoint, the amount of rain that can be observed falling into this footpoint is minimal and is also very faint.

The last path, path 10, may also belong to the large loop bundle of region 1, and the location of its footpoint is uncertain. In contrast to the region in which the previous paths are rooted, path 10 appears to be rooted in moss. Minimal rain events are seen in this case.

All rain tracks observed in region 2 mostly show EUV absorption, with little EUV emission of the type described earlier that is associated with compression. Moreover, most tracks are relatively short (10−20 Mm) when compared to region 1, which may be due to the different inclination of the loops relative to the LOS.

4.8. SPICE view of regions 1 and 2

The SPICE rasters captured part of the regions of interest observed with HRI_{EUV} on April 1st. This includes the top part of region 1 and most of region 2 (see Fig. 2, bottom), which mostly correspond to the apexes of the loops with coronal rain. These loops are barely visible in the Mg IX coronal line (Fig. A.2), but their filamentary structure is clearly visible in the upper TR lines (Ne VIII and O VI in Figs. A.3 and A.4). Furthermore, emission similar in morphology and strong variability is also visible in the lower TR N IV line (Fig. 12). For instance, the large-scale brightening in the loop that corresponds to paths 1 to 5 in region 2 (described in Sect. 4.7) peaks in Mg IX at UT 09:36 (red arrow in the corresponding figure), while in Ne VIII, O VI, and N IV, the brightening peaks at UT 09:52, and in C III, the peak is visible at UT 10:06 (with some hints of increased brightness in Lyman-β as well, but this is inconclusive due to the strong background). This strongly supports our interpretation of cooling through the passbands of HRI_{EUV} and SPICE and subsequent appearance of rain in EUV absorption.

4.9. Region 3 of April 1st: Localised and large-scale flash-like EUV emission from rain

Figure 13 shows region 3, as denoted in the full FOV of Fig. 1 (right panel), with several rain paths overlaid. Most of the loops analysed in region 3 show a very different inclination with respect to the LOS when compared to the previous cases. In this case, the LOS appears much less inclined with the loop plane, leading to a top view of the loop rather than a sideways view. Consequently, while the footpoint legs appear to be very short, the apexes appear to be long in the projected view.

Paths 1−6 appear to correspond to the same loop bundle, although paths 4−5 show slightly different trajectories relative to paths 1−3, which may be indicative of braiding. This is further supported by the AIA observations of the same event, as discussed in Sect. 4.13. In the loops in region 2, a strong EUV enhancement uniformly along several coronal strands composing the loop bundle is visible roughly 10 min from the start of the observation. The coronal strands appear to be extremely thin, with sub-arcsecond widths (see Sect. 4.12). This brightening can be clearly seen in the time-distance diagrams shown in Fig. B.3. Most of the coronal strands disappear 20 min later. Both dark and bright tracks can be seen in most time-distance diagrams, which is indicative of flows in both directions (towards both footpoints). Some tracks appear at the start of the global intensity enhancement, and others appear 20−60 min after. We note that despite the very close proximity of paths 1 and 2 and paths 4 and 5, they show different (dim) features in their evolution. AIA 304 confirms the presence of rain in this loop bundle (Sect. 4.13).

Path 3 corresponds to one of the best visible coronal strands. As shown in the time-distance diagram, no clear bright or dark track can be seen. We selected this path to more accurately investigate the uniform global intensity enhancement common to many of the strands in the loop bundle. In Fig. 14 (top) we show the part of the time-distance diagram corresponding to the intensity enhancement for path 3. Compared to the background,

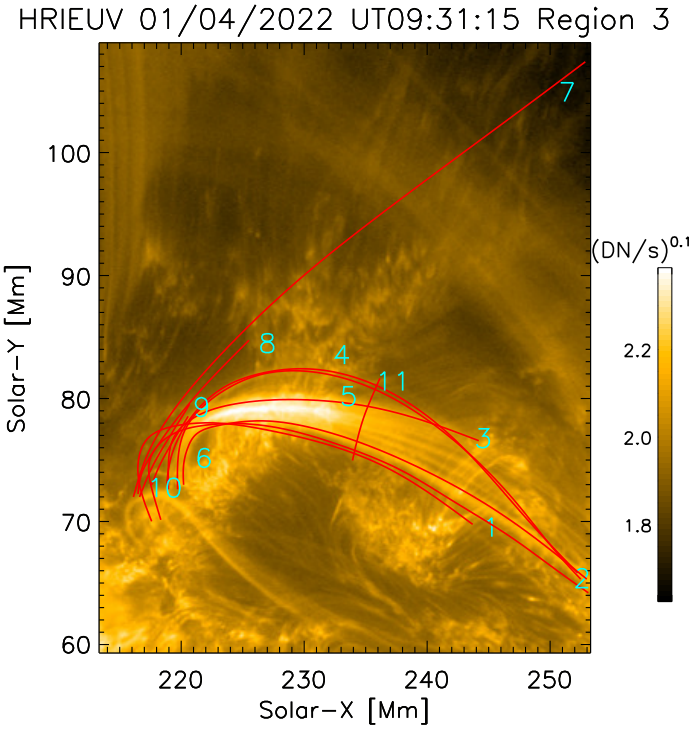

Fig. 13. FOV of region 3 shown in Fig. 1 (right panel). The red curves correspond to paths of some of the observed coronal rain clumps. Paths 1 to 6 belong to the bright loop in the lower half of the image, and paths 7 to 10 belong to a very long loop that extends towards the top right corner of the image. Paths 9 and 10 are very short and parallel to each other. We note that the intensities are scaled with a power of 0.1 to show a wider range of variations. An animation of this figure is available online, whose images have been processed with the wavelet-optimised whitening enhancement technique of Auchère et al. (2023). It runs from UT 09:19 to UT 10:34 and shows several brightenings followed by mostly bright rain clumps falling towards the chromosphere. The movie first runs without and then with the rain paths overlaid.

the enhancement appears to be diffuse and seems to start close to the apex. It propagates towards both footpoints in several minutes. Overall, this global intensity enhancement over the strand lasts ≈8 min. In Fig. 14 (bottom) we show a similar case for path 2. However, in this case, about four intensity enhancements are observed, and almost all are accompanied by dark or bright propagating features.

Although many of the features in paths 1−6 do not show the EUV absorption but rather emission, we still associate them with coronal rain. In addition to similar velocities (see Sect. 4.11), the AIA observations of the same event provide conclusive proof (Sect. 4.13).

The last set of paths we analysed are paths 7−10, which correspond to a different loop that apparently is much larger. We were able to track a bright clumpy feature over 40 Mm, leading to path 7. The clump falls at speeds of ≈150 km s^{-1} in the POS, which to our knowledge is the fastest ever recorded speed for a falling clump with imaging devices (except for erupting fallback). Just prior to impact, over the last 5−15 Mm, several other clumps are seen along parallel paths (tracks in paths 8, 9, and 10), suggesting that the catastrophic cooling to chromospheric temperatures takes longer for these neighbouring strands.

In Fig. 15 we show a close-up of the time-distance diagram corresponding to paths 7 (top) and 10 (bottom) over the time where the falling clump is observed. The bottom panel in the

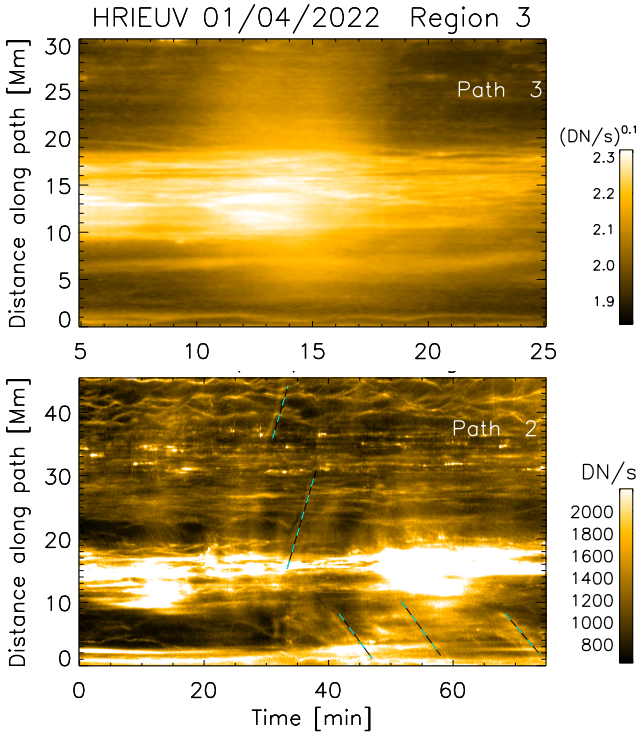

Fig. 14. Loop brightening and downflows along the loop bundle in region 3. Top: loop brightening prior to a coronal rain event. This time-distance diagram (close-up of the time range $t = [5, 25]$ min) corresponds to path 3 in region 3 on April 1st, which is shown in Fig. B.3. We note that the intensities have been scaled to the power of 0.1 to show the large intensity variation better. Bottom: time-distance along path 2 in the same loop bundle. The dashed white lines correspond to dark and bright tracks from coronal rain.

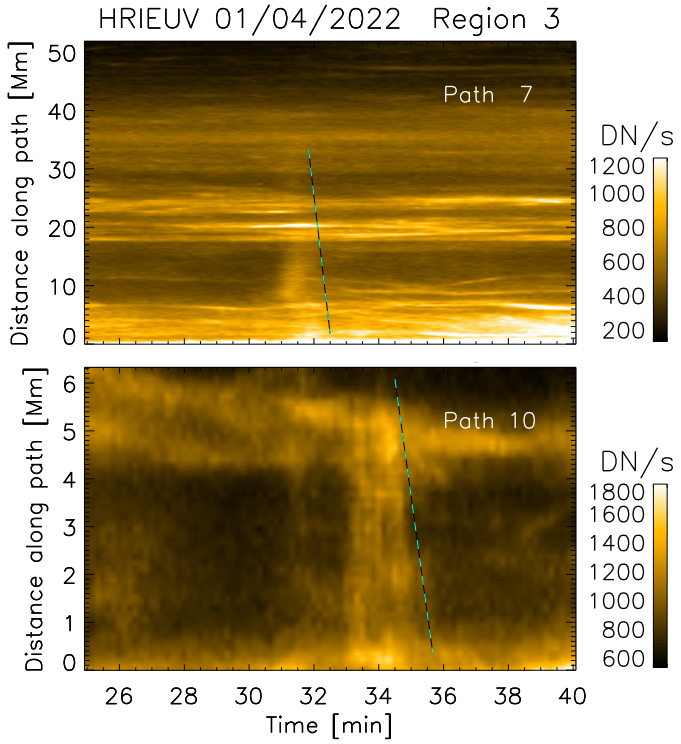

Fig. 15. Close-up of the time range $t = [25, 45]$ min in the time-distance diagram of paths 7 (top) and 10 (bottom) shown in Fig. B.3. We note that the beginning of the brightening at $t \approx 33$ min starts essentially at the same time along the path. The dashed cyan-black lines trace the outer envelope of the brightening, indicating a speed of $\approx$150 km s^{-1}.

figure shows a very interesting pattern. While the outer envelope (traced by the dashed cyan-black line in the figure) corresponds to the same speed as observed in the longer time-distance path of path 7 (top panel), there is an almost instantaneous intensity increase all along the path at time $t \approx 33$ min. This feature is probably due to the compression of the rain downstream, that is, it is physically similar to the small brightening observed for the March 30 rain clumps. However, while the brightening for the latter is always immediately below the head of the rain, in this case, it occupies a much larger longitudinal extent. This is probably due to a much stronger compression, which is able to increase the temperature of the entire region below the rain to a temperature close to the emissivity peak of HRI$_{\rm EUV}$ ($\log T = 5.8-6$), thereby generating a flash effect.

4.10. Region 4: Off-limb coronal rain

On April 1st, HRI$_{\rm EUV}$ captured various long loops rooted in the trailing AR closer to the limb. Small EUV absorption features falling towards the surface are visible in one such loop, which we followed and show in red within region 4 shown in Fig. 1. The time-distance diagram along this path is shown in Fig. 16, where various characteristic dark and bright tracks of coronal rain can be seen to fall at projected speeds of 50–90 km s^{-1}. This loop is also partly visible in the SPICE rasters of April 1st. In Figs. A.7–A.11 we show the evolution through the SPICE rasters of the emission in this region. In particular, we note strong variability in the upper and lower TR (Ne VIII, O VI, and N IV) and chromospheric emission (C III and Lyman-β), as shown in Fig. 17. Therefore, SPICE confirms the presence of coronal rain emitting at TR and chromospheric temperatures in this loop.

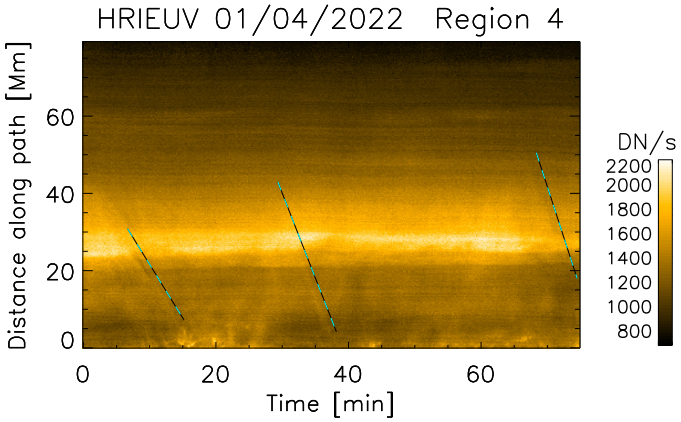

Fig. 16. Time-distance diagram along a loop observed partly off-limb by HRI$_{\rm EUV}$ on April 1st. The path corresponds to red curve in region 4 shown in Fig. 1. The dashed cyan and black lines correspond to dark and bright tracks from coronal rain (offset in time by 1 min in the figure for clarity).

4.11. Statistics

In this section, we provide statistics of all the velocity and width measurements of the coronal rain clumps (both in absorption and in emission). We refer to Sect. 3 for the methods with which these quantities were calculated.

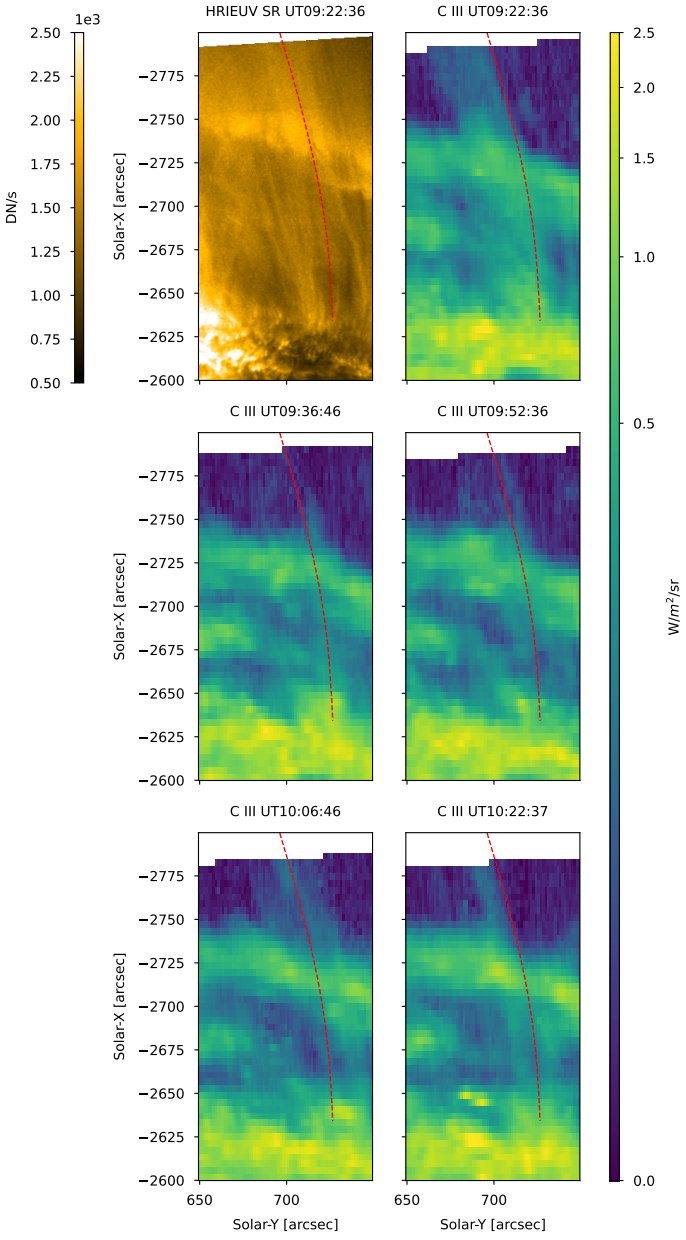

Fig. 17. SPICE rasters in the C III line ($\log T = 4.8$ K) over a region that overlaps with region 4 on April 1st. The FOV corresponds to the red rectangle to the east shown in Fig. 2 (bottom), and the overlaid red curves denote some of the rain paths seen with $\mathrm{HRI_{EUV}}$ (see Figs. 10 and 11). The $\mathrm{HRI_{EUV}}$ panel corresponds to an SR matching the time of the first SPICE raster (see the text for details), but preserving the $\mathrm{HRI_{EUV}}$ spatial resolution. The SPICE panels show the total intensity integrated over the C III spectral line for each raster (the time is shown in the subtitle).

In Fig. 18 we show a histogram of all the measured projected velocities for both datasets. We note that the peak of the distribution is between 40 and 60 km s^{-1}, with speeds as low as 10 km s^{-1} and as high as 150 km s^{-1}. The latter high projected velocities are not common for coronal rain, and they may well constitute the highest projected velocities to date (we note that eruptive prominence fallback is not coronal rain). No great differences exist between the two dates, except that April 1st presents a wider spread, which is normal because we analysed more rain events for that date. The bulk of the distribution matches previously reported speeds wee (Antolin & Rouppe van der Voort 2012; Schad 2017;

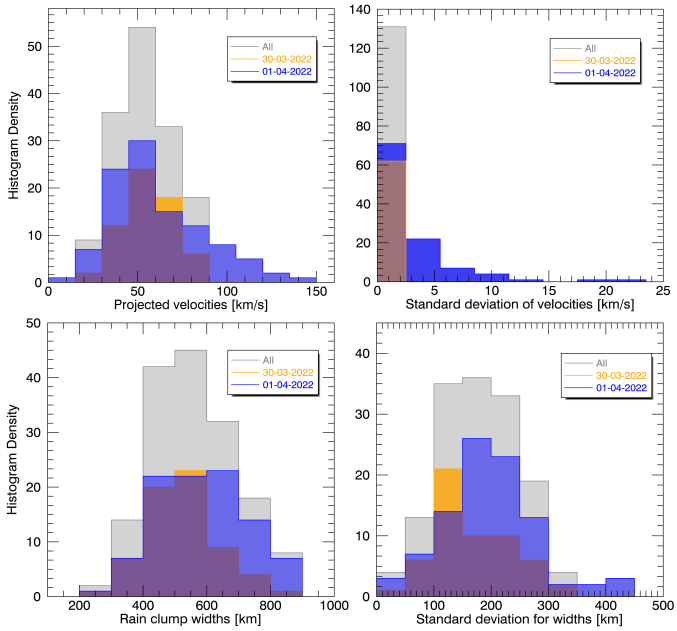

Fig. 18. Projected velocities (top), widths (bottom), and associated standard deviation (corresponding to the right panels) for all rain clumps. The colours include transparency and denote different dates (see legends).

Antolin & Froment 2022), and it also matches those obtained in numerical simulations (Fang et al. 2015; Li et al. 2022). As shown in the figure, the errors on the velocity measurements are generally small (about 5 km s^{-1} for most).

Similarly, in Fig. 18 we show a histogram of all measured rain clump widths. The distribution peaks between 400–600 km, but extends as low as 260 km and as high as 890 km. Both dates present small differences in terms of the distribution shape. While both datasets have relatively small pools, the dataset of April 1st presents a broader distribution, with values that are higher by about 100 km. The standard deviation figure indicates that the error in the width measurement is relatively large. This is expected because along a given track, the rain clump background varies significantly, leading to differences in the results of the Gaussian fits (despite efforts to reduce the background influence; see Sect. 3).

4.12. Coronal strands associated with coronal rain

To investigate the possible relation between the filamentary coronal structure (coronal strands) within loop bundles and the coronal rain they host more carefully, we took cuts across several of the analysed loop bundles, as shown in Figs. 5 (path 11), 10 (path 8), 11 (path 11), and 13 (path 11). We show the resulting time-distance diagrams along these cross cuts in Fig. 19.

Several coronal strands are shown in each figure, some of which very likely belong to the loop bundle hosting the rain event. In many instances, as the rain crosses the transverse cuts, it produces a small absorption feature (whose time duration depends on the clump length and speed). One example of such a feature is shown by an arrow in Fig. 19. It is preceded and followed by a bright EUV feature of roughly the same width as the rain clump. A large group of rain clumps is seen around $t = 22$–32 min, followed by a bright feature at $t = 32$–40 min.

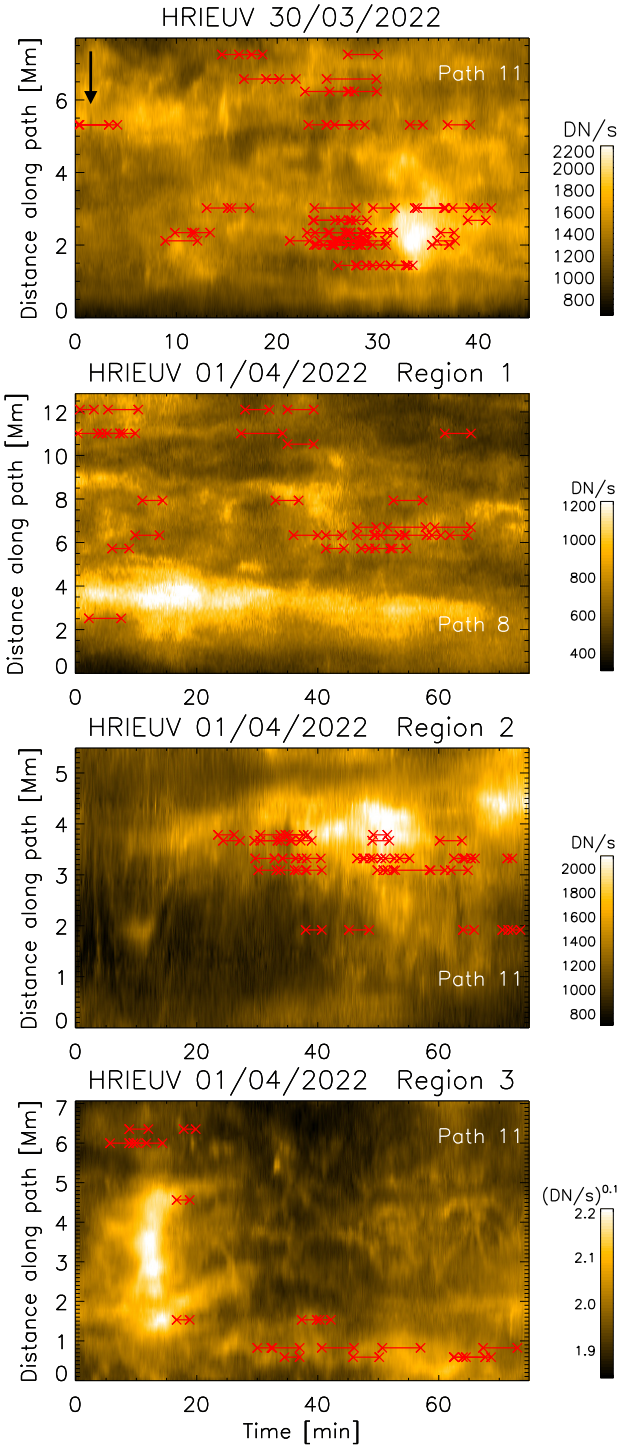

Fig. 19. Time-distance diagram along paths that cross several loop bundles: Path 11 in Fig. 5 (top), path 8 in Fig. 10 (second panel from top), path 11 in Fig. 11 (third panel from top), and path 11 in Fig. 13 (bottom). The red lines between crosses denote the times and the location at which rain clumps are observed. The vertical black arrow in the top panel indicates an example of an EUV absorption feature produced by a rain clump. The intensities in the bottom panel have been scaled to the power of 0.1 to show the strong intensity variation better.

This bright feature corresponds to the rebound shock and upward flow produced by the impact of the rain shower.

In Fig. 19 a group of strands appears after $t = 30$ min between distances of 5 and 8 Mm across the transverse cut. It seems to coincide with the location in time and space of a group of rain clumps. Similarly, in the other panels in the figure, the rain clumps appear to be preferentially located in regions where coronal strands are observed. While a one-to-one association between a coronal strand and a rain clump can sometimes be made (particularly for the latter), this is not generally the case. However, the widths of coronal strands (around 500 km) are similar to those of rain clumps on average.

4.13. SDO/AIA observations at different lines of sight and resolutions

Our investigation of the coronal rain events with HRI_{EUV} was complemented by co-temporal SDO/AIA observations. On these dates, Solar Orbiter was in quadrature with SDO, thereby offering a different view of the same ARs. In Figs. 20 and 21 we show snapshots for March 30 and April 1st, respectively, with a FOV centred on the regions of interest. The same large-scale coronal structures can be identified in the data from both instruments.

Despite the similarity between AIA 171 and HRI_{EUV} in terms of the emission and the large-scale nature of the event (occurring across at least 15 Mm in HRI_{EUV}), no clear downflow can be observed in absorption or emission with AIA 171 on March 30 over the same time period. Sections of the loop bundle appear and disappear over the same duration, which likely correspond to the EUV variation associated with coronal rain observed with HRI_{EUV}. Some upward flows, bright in the EUV, are observed, which could correspond to the rebound shock and flow observed with HRI_{EUV}. To verify this, we identified and tracked a few large rain clumps in AIA 304, whose paths are shown in Fig. 20. The time-distance diagrams along these paths are shown in Fig. 22, and the characteristic rain slopes in AIA 304 are easily identified (tracks in the time-distance diagrams). We note the brightenings at the times the rain impacts the chromosphere. With the help of AIA 304, the rain features in AIA 171 can be recognised, such as EUV absorption, and in particular, a rebound shock and flow feature following the rain impact. The strong EUV variation that is seen in the image sequence is therefore attributable to the rain episode.

On April 1st, only region 1 shows clear coronal rain in the image sequence of AIA 171, with the characteristic EUV absorption features downflowing along the loop. Regions 2 and 3 show very similar EUV variation as was observed with HRI_{EUV}, but as for March 30, we were unable to directly identify coronal rain downflows based on the EUV absorption features in the image sequences alone. However, the expected coronal rain is revealed in the 304 channel, and we were able to roughly identify the large-scale coronal rain events for each of the loops. In the data from March 30, we tracked several large rain clumps in each region (shown in Fig. 21) and plot the time-distance diagrams in Fig. 23. Path 1 tracks a rain clump belonging to the loop in region 1, paths 2 and 3 belong to region 2 and may correspond to the loops outlined by paths 8 and 9 in Fig. 11, and paths 4 and 5 follow clumps in the loop bundle outlined by paths 1 to 6 in Fig. 13. We are able to detect several rain tracks in the time-distance diagrams of AIA 304 and a very clear EUV absorption profile in AIA 171 for path 1. However, the signatures in AIA 171 are much harder to detect. In paths 2 and 4, we do not see any features of the rain falling in AIA 171, but a bright feature can be seen near the footpoint of path 4 that may correspond to the impact and rebound shock and flow from a rain shower. In paths 3 and 5, we are able to recognise a few EUV absorption and emission tracks that are co-temporal and co-spatial to the rain tracks in AIA 304. The bright EUV emission in 171 is similar to that seen in HRI_{EUV} in paths 1 or 6 of Fig. B.3,

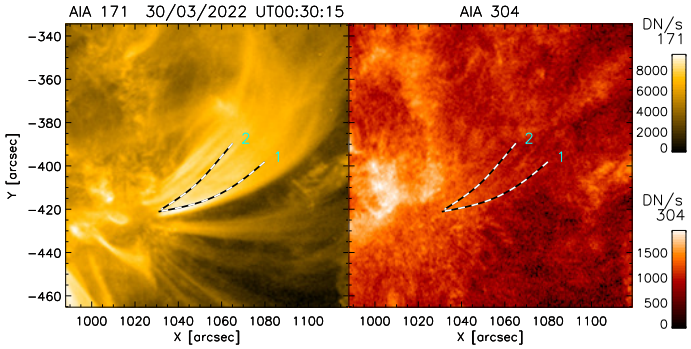

Fig. 20. SDO/AIA observation in the 171 (left) and 304 (right) channels of the March 30 coronal rain event. AIA was roughly in quadrature with Solar Orbiter on this date. The large loop bundle observed in the AIA 171 map corresponds to the same loop bundle as was observed by HRI_{EUV} in Fig. 5. The dashed white-black paths follow some rain clumps observed in AIA 304. An animation corresponding to this figure is available online. The animation shows several rain clumps in AIA 304, but no clear counterpart is seen in AIA 171, although strong intensity variations are observed at the same locations. The animation runs from UT 00:02 to UT 00:49 and comprises the time where coronal rain is observed with HRI_{EUV}. It first runs without and then with the rain paths overlaid.

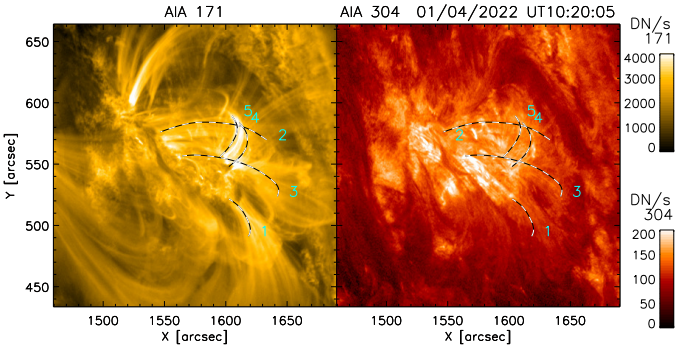

Fig. 21. SDO/AIA observation in the 171 (left) and 304 (right) channels of the April 1st coronal rain events. AIA was roughly in quadrature with Solar Orbiter on this date. Some of the large loop bundles observed by HRI_{EUV} can be easily identified. The dashed white-black paths follow some rain clumps belonging to these loop bundles that are observed in AIA 304. Path 1 follows the same loop bundle as in region 1 of Fig. 10. Paths 2 and 3 may correspond to the same rain events that were shown in paths 8 or 9 in region 2 of Fig. 11. Paths 4 and 5 follow the same loop bundle as was shown in the lower part of Fig. 13 (paths 1 to 6 in that figure). An animation corresponding to this figure is available online. The animation shows widespread rain in AIA 304, but the counterparts in AIA 171 can only clearly be seen for the loop around path 1, although strong intensity variations are observed at the same locations. The animation runs from UT 09:20 to UT 10:32 and comprises the time where coronal rain is observed with HRI_{EUV}. It first runs without and then with the rain paths overlaid.

in which large-scale emission is seen simultaneously throughout the path, which precedes the bright downflowing feature from the rain.

It is interesting to note that as shown by the AIA 304 animation, coronal rain over the AR is widespread over the same FOV as HRI_{EUV} and that it includes loops for which it is not observed with HRI_{EUV}. A large amount of coronal emission ahead of the rain along the LOS can easily decrease the contrast produced by EUV absorption or emission from the rain in the 171 or 174 channels, thereby making it undetectable. As we show here,

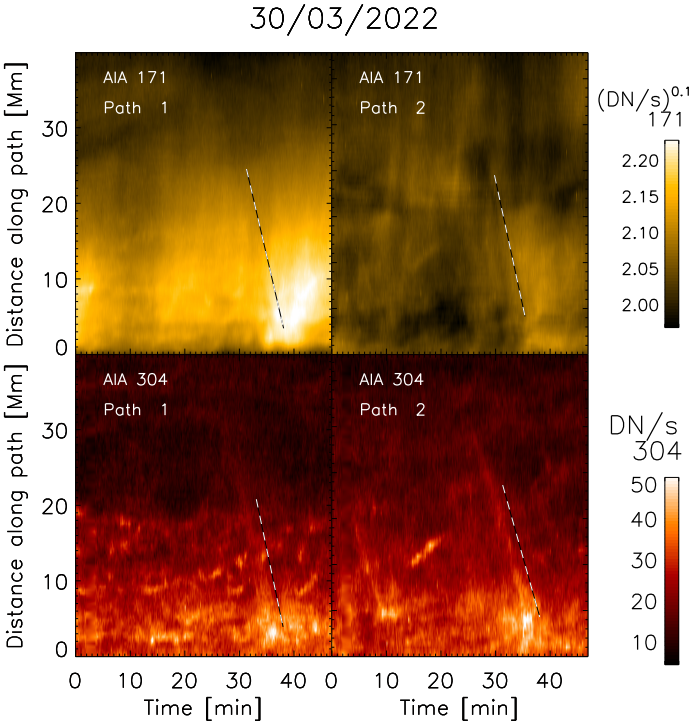

Fig. 22. Time distance diagrams along paths 1 and 2 shown in Fig. 20 on March 30, with AIA 171 (top) and AIA 304 (bottom). The dark and bright paths from coronal rain are highlighted with dashed white-black lines, which are offset by a fraction of a minute to show the rain features better. Zero distance corresponds to the footpoints of the loops. The AIA 171 intensities have been scaled to the power of 0.1 to show the strong intensity variation better.

high spatial resolution can help us to retain this contrast, which is why we observe far more in HRI_{EUV} than AIA 171. On the other hand, AIA 304 shows the emission or absorption from the rain more directly because no further emission is present ahead of the rain along the LOS. Nevertheless, the rain can be hard to discern due to the very bright TR background in AIA 304.

The larger FOV provided by SDO/AIA sheds more light on the large-scale magnetic structure of region 1 on April 1st. AIA 171 reveals a topology that is similar to a null-point topology, with open field lines (or much larger loops) above and the loop arcade below the null-point. This provides an explanation for both the large-scale reconfiguration and the observed large-scale coronal rain event in the loop, with continuous coronal rain over a very wide loop cross-section observed for the entirety of the HRI_{EUV} observation. As discussed in Li et al. (2018) and Mason et al. (2019), magnetic dips are often observed above null-point topologies, which act as mass reservoirs where large amounts of material can catastrophically cool down. The cool and dense material can then either spill sideways from the magnetic dip or flow through the null-point, facilitated by the reconnection process, downward into the newly formed reconnected loops. This process can be very long-lived (Chitta et al. 2016; Chen et al. 2022) and can be accompanied by a reconfiguration of the loop, similar to shrinkage (as in the standard flare model).

4.14. Widespread coronal rain as suggested by SPICE

All the loops with coronal rain captured with HRI_{EUV} show clear counterparts in SPICE in the upper and lower TR lines. For the off-limb loop in region 4, we were also able to capture

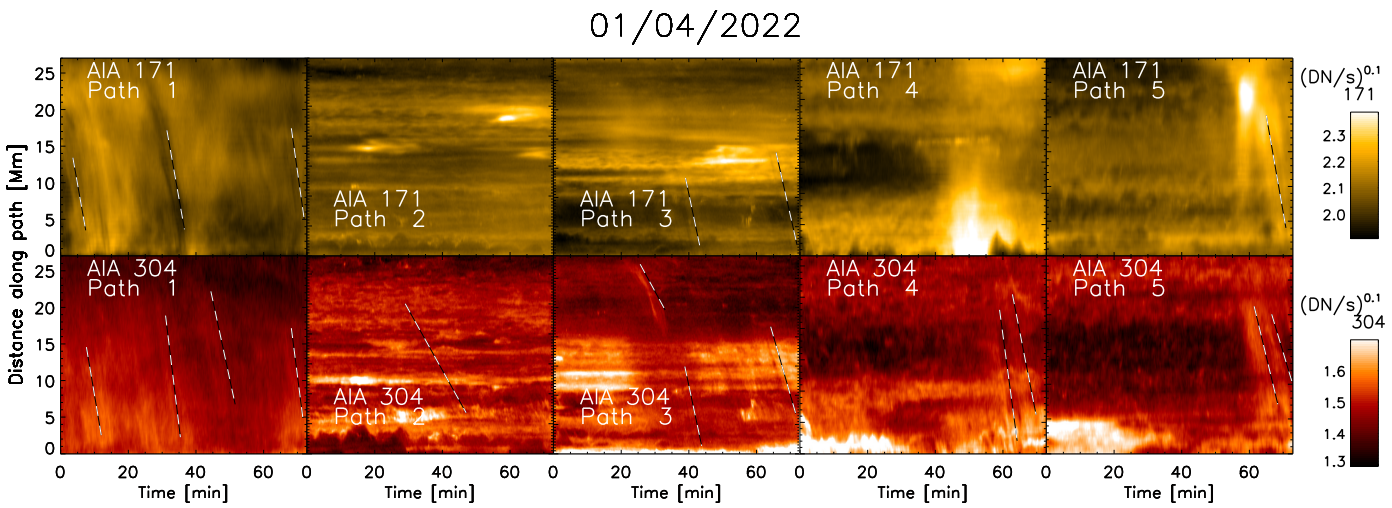

Fig. 23. Time-distance diagrams along paths 1 to 5 shown in Fig. 21 on April 1st, with AIA 171 (top) and AIA 304 (bottom). The dark and bright paths from coronal rain are highlighted with dashed white-black lines, which are offset in time by 1 min to show the rain features better. Zero distance corresponds to the footpoints of the loops. The intensities have been scaled to the power of 0.1 to show the strong intensity variation better.

clear emission in the chromospheric lines of SPICE because the background emission was lower. In Fig. 24 we show a multi-wavelength view of the full FOV of SPICE for one raster. Widely spread cool loops emitting in the upper and lower TR lines, with features (morphology and variability) similar to those for which we detected coronal rain, are visible in the FOV. All the five rasters of this region show strong variability in these loops. This strongly suggests that at least for this AR, coronal rain is widely spread and that only a fraction of it is observed in EUV absorption with $\mathrm{HRI_{EUV}}$. This also matches the picture obtained with AIA 304.

5. Discussion and conclusions

We analysed coronal rain at unprecedented spatial resolution in the EUV, provided by Solar Orbiter observations with $\mathrm{HRI_{EUV}}$ during the March and April 2022 perihelion. Observations were complemented with SPICE and AIA, providing a multi-wavelength picture of the phenomenon in various active regions. The resolution achieved is ≈240 km, which is only about two times lower than previous Hα observations of the phenomenon with the SST (Antolin & Rouppe van der Voort 2012). The strong correlation between EUV absorption and Hα emission that is expected from radiative transfer theory (Anzer & Heinzel 2005) is confirmed here down to the smallest resolved scales ever achieved, with clump FWHM widths as small as 260 km. This fine-scale structure is also reflected in the fact that many clumps only produce very faint EUV absorption features, thereby requiring high-resolution and sensitivity to detect them.

We selected two dates on which Solar Orbiter observed several ARs on-disk and partly off-limb. For March 30, we focused our attention on one coronal loop bundle and discovered new features of coronal rain dynamics. As the rain falls, the region immediately beneath the clump (downstream) is observed to brighten, leading to very fine light streaks in time-distance diagrams. We interpret this phenomenon as the result of compression and heating due to the relatively high momentum of the condensation. Fang et al. (2015) reported the formation of rebound shocks when coronal rain forms that is produced by the localised loss of pressure driving strong flows that lead to the condensation. These rebound shocks may be thought of as the source of the brightening that we see. However, the rebound shocks are then seen to propagate away at the sound speed from both sides of a condensation, much faster than the condensation falling speeds. There is no reason why these rebound shocks should propagate at the same speed. Therefore, these rebound shocks cannot explain our observations. On the other hand, our interpretation as compression and heating is supported by 2.5D MHD simulations of coronal rain by Li et al. (2022, see their Fig. 4) and Antolin et al. (2022). This phenomenon is therefore similar to the fireball phenomenon on Earth that is linked to meteoric ablation, where the region below the clump is compressed and heated as it falls. We do not observe this phenomenon for all coronal rain events, which suggests that not only a high spatial resolution is needed, but also a favourable line of sight relative to the rain trajectory. It is also possible that the compressed material exists in all cases, but emits at different temperatures that are not sampled by $\mathrm{HRI_{EUV}}$.

EUV enhancement associated with coronal rain is also observed during the fall ahead and in the wake of rain clumps. The latter can be seen in the time-distance diagrams along or across rain clump trajectories as an increase of the EUV intensity that follows the EUV absorption feature. This may correspond to a coronal strand and is likely due to the CCTR, which extends from the clump far into the wake, as shown by numerical simulations (Antolin et al. 2022; Li et al. 2022). Observations with SPICE show the filamentary structure in the upper and lower TR lines, which supports this interpretation. Ahead of the clump, a second more elusive type of brightening is observed in addition to the fireball feature, just prior to the rain impact (the brightening spreads over ≈6 Mm), and it manifests as a flash-like simultaneous intensity enhancement of the entire space between the clump and the chromosphere. We suspect that this is also due to the compression of the plasma ahead of the clump, as suggested by the same numerical simulations cited previously. The compression must be strong enough to increase the temperature of the entire region below the rain close to the emissivity peak of $\mathrm{HRI_{EUV}}$ ($\log T = 5.8$–6), thereby generating a flash effect. However, we only found one clear occurrence of this larger-scale compression for which the rain is extremely fast (with projected speeds of 150 km s^{-1}). These speeds may be supersonic, in which case the compression argument may not fully explain it.

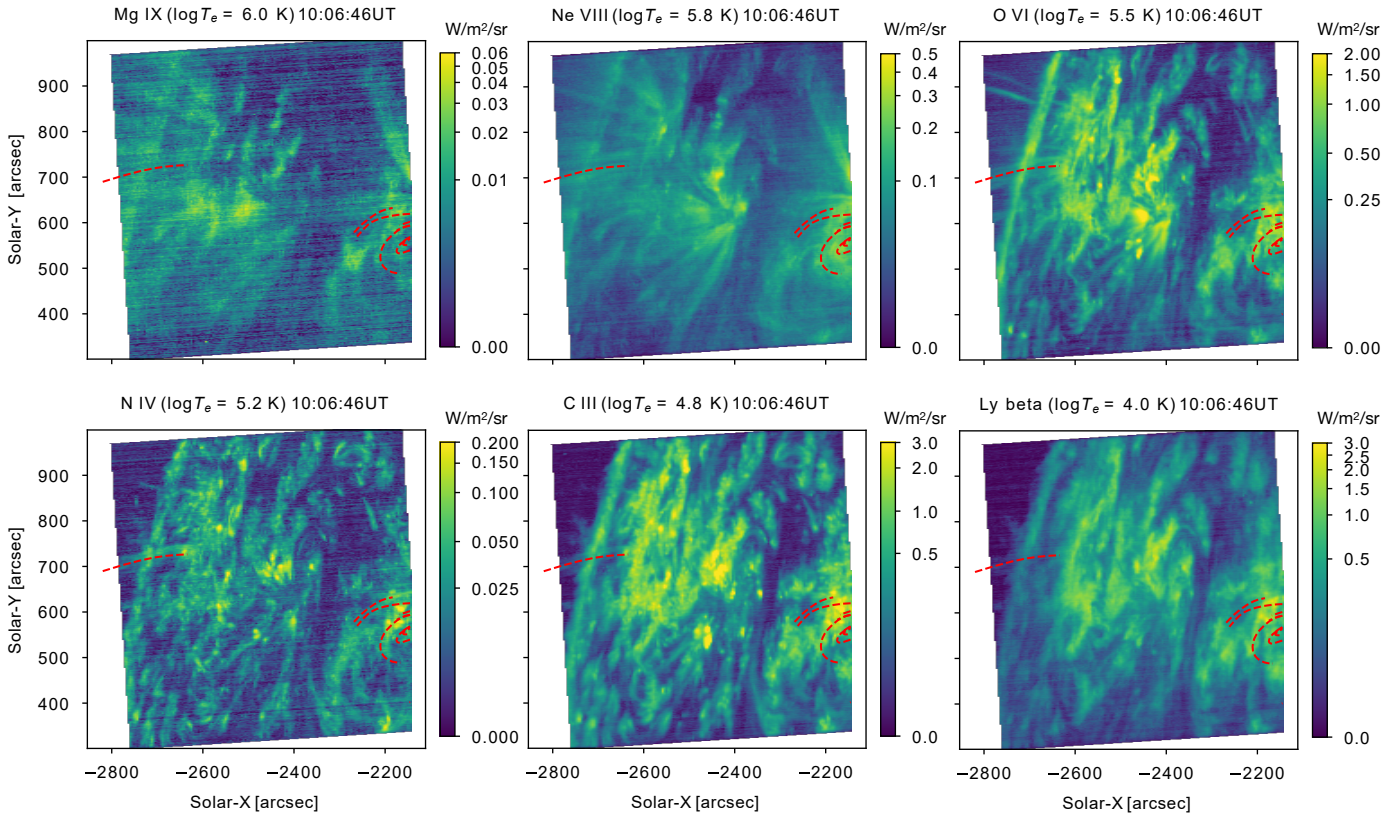

Fig. 24. SPICE multi-wavelength full FOV on April 1st. The SPICE FOV is the same as was shown in Fig. 2 (bottom), co-aligned with HRI_{EUV}. The overlaid red curves denote some of the rain paths seen with HRI_{EUV} (see Figs. 10 and 11). Each SPICE panel shows the total intensity over a spectral line indicated in the subtitle, together with its temperature of maximum formation.

If it is indeed produced by compression, this means that sound waves are produced ahead of the clump and travel fast enough to compress the entire region donwstream (leading to the flash-like character of the brightening). However, this is not possible if the clumps are supersonic.

Another new phenomenon is the rebound shock and upflow that follows the rain impact into the chromosphere. The feature is detected best after the end of rain showers rather than in individual rain clumps, and it is characterised by a bright and diffuse propagating EUV feature roughly along the same paths on which the cool downflows occur. The propagating speeds are between 50 and 130 km s^{-1}, depending on the selected path for the time-distance diagram. Based on multi-dimensional simulations of this phenomenon (Antolin et al. 2022), we suspect that this difference is due to the combination of the rebound shock, which propagates at a tube speed of ≈130 km s^{-1} (for temperatures corresponding to the Fe X 174 Å formation temperature of $10^{5.98}$ K), and an upward flow produced by the impact (which are bound by gravity and thus slower). To the best of our knowledge, this is the first report of this effect, although it has been predicted by numerical simulations for decades (Mendoza-Briceño et al. 2002; Müller et al. 2003; Antolin et al. 2010; Fang et al. 2015; Li et al. 2022). We expect a response from the lower atmosphere in the form of an upflow or upward-propagating wave along every magnetic field line and probably even over a wider region than is affected by the rain impact because of the high-β conditions and strong gas pressure increase at the chromospheric heights of rain impact (Antolin et al. 2022). For the March 30 event, this upward-propagating feature is seen to reheat the loop bundle and may correspond to the start of a new TNE cycle. Simulations indicate that efficient refilling and reheating of the loop is only obtained when the stratified heating is still ongoing. In other words, if there is no continuous heating at the loop footpoint, the simple rebound shock and flow obtained from a rain shower is insufficient to return the density and temperature to usual coronal values. The rebound shock and upflow can be seen mainly after rain showers rather than individual rain clumps, suggesting an additional feedback effect from the high rain shower momentum. Only a subset of rain showers shows these features, despite their relatively large-scale nature, indicating that the conditions for observing this atmospheric response to the rain impact are stringent. This is further supported by the AIA 171 co-temporal observations on March 30 in quadrature with HRI_{EUV}, where some hints of an upward-propagating disturbance are observed, but they remain much dimmer and elusive.

As shown by Şahin & Antolin (2022), rain showers can help us identify coronal loop entities (defined as a coronal volume evolving in similar way and therefore subject to similar heating conditions). This is particularly important given the optically thin nature of the corona, which leads to great LOS superposition (also referred to as 'the coronal veil'; Malanushenko et al. 2022). Furthermore, the occurrence of coronal rain points to a state of TNE for which stringent coronal heating conditions are needed. This is particularly the case of quiescent coronal rain, which occurs in usual coronal loops and is accompanied by long-period intensity pulsations for long-duration heating (Froment et al. 2020). It is still unclear whether the TNE-TI scenario still applies to prominence-coronal rain hybrid structures (although initial results indicate a quasi-periodic occurrence

that may correspond to long-period intensity pulsations; Li et al. 2019) or even to flare-driven rain.

Klimchuk & Luna (2019) have quantified the conditions for TNE, which include a strong heating stratification (ratio of apex-to-footpoint volumetric heating rate below 0.1) and not too high heating asymmetry between footpoints (below 3, to prevent siphon flows that effectively reduce the lifetime of the condensations in the corona relative to their falling time). Johnston et al. (2019) further showed that a high-frequency rate for the heating events (with a repeating time shorter than the radiative cooling time of the loop) is needed. Several of the observed rain showers in this work occur following a global brightening of the loop. This is expected from the TNE-TI cycle, in which the loops start at a hot indeterminate temperature and cool down radiatively. What is observed then corresponds to the loop temperature experiencing the temperature response range of the HRI_{EUV} channel, which peaks at $\approx 10^6$ K (Rochus et al. 2020). The usual draining and cooling of loops would explain this global brightening feature, but would fail to explain the appearance of the clumpy downflows in EUV absorption or emission that follow the global brightening events (Peter et al. 2012). This is also the case in post-flare cooling, where simple draining and global cooling of loops is unable to explain flare-driven rain (Reep et al. 2020). Our cooling interpretation is further supported by the SPICE observations, which show that the brightening is delayed for cooler spectral lines at TR and chromospheric temperatures.

It is interesting to note that the observed global brightening occurs fairly uniformly and symmetrically along the loop. The apex brightening occurs a few minutes prior to the rest of the loop. To our knowledge, very few works have investigated (including the necessary forward modelling into e.g. AIA 171) the spatial distribution of the cooling during TNE cycles in detail. The literature indicates that we should expect symmetric global brightening in a channel such as AIA 171 during the cooling stage of TNE cycles when the heating is symmetric at both footpoints (Müller et al. 2003; Peter et al. 2012; Winebarger et al. 2018; Johnston et al. 2019), while asymmetric heating or the loop geometry may tend to produce asymmetric global brightening, with significant brightening only along one loop leg (Mikić et al. 2013; Froment et al. 2018; Pelouze et al. 2022). This would suggest that both the heating along the observed loops with rain and the geometry of these loops are symmetric rather than asymmetric.

In our observations, the rain is observed to occur in some cases immediately after the global loop brightening (within about 10 min), while other cases show a longer waiting time (over 40 min), which indicates different average loop densities. While some clumps are seen to fall over large distances over 40 Mm, most only appear in the last 10−20 Mm. This spatial occurrence of coronal rain is often the case when the heating or loop geometry is asymmetric because these configurations generate siphon flows that reduce the lifetime of the cooling plasma in the loop, also leading to what is known as incomplete condensations that do not appear in chromospheric lines (Mikić et al. 2013; Froment et al. 2018; Pelouze et al. 2022). Hence, in contrast to the argument in the previous paragraph, this would suggest asymmetric heating or loop geometries. This contradiction suggests another possibility. For instance, it is also possible that the better visibility of the condensations with decreasing height is due to a simple LOS effect because we expect a higher column mass of cool material along the LOS (and therefore stronger EUV absorption) closer to the footpoints. This is supported by the SPICE observations, which show cool emission down to low TR temperatures (or even lower temperatures) along the loops with rain.

Another interesting point is that the height at which the condensations occur seems to decrease the farther away we are from the largest or clearest clumps (those producing the clearest EUV absorption features). This behaviour suggests progressive and non-uniform cooling across the loop, which may reflect slightly different conditions, such as the field line length and differences in the heating that ultimately affect the character of the thermal instability (as seen in numerical simulations; e.g. Froment et al. 2018; Pelouze et al. 2022).

Some showers occur over a very wide volume, over 15−20 Mm in the POS. This is a lower estimate because the loops are observed to expand and most rain clumps appear closer to the footpoint, over the last 10−20 Mm lengths prior to impact. The SPICE observations confirm this because the loops appear to be wider in the cool TR lines. The footpoint of these loop bundles is relatively wide (4−10 Mm, as shown in Figs. 5, 10–13). This suggests similar heating conditions in a relatively wide region (several times the granular scale) and probably a locking or synchronising mechanism that can act over wide distances across the magnetic field. Thermal instability has been suggested for this synchronising role (Antolin & Froment 2022).

The width distribution for rain clumps peaks at $\approx 500 \pm 200$ km. At the smaller range of this distribution, we have the widths observed in Hα with the SST or GST (Froment et al. 2020; Jing et al. 2016), while the wider range is common for the widths observed in chromospheric and TR lines with IRIS (Antolin et al. 2015; Şahin et al. 2023). Not much variation is observed across different regions. This little variation has been reported in Şahin et al. (2023) and suggests a more fundamental nature of the plasma morphology in MHD. These widths might be governed by the underlying magnetic topology and/or by the length scales of the heating (Antolin et al. 2022). However, they can also be associated with thermal instabilities (Antolin et al. 2015; Claes & Keppens 2019; Claes et al. 2020). We have shown that very sharp bright coronal strands appear to be co-located with the rain clumps within the loop bundle and exhibit very similar widths of ≈500 km, consistent with the widths of coronal sub-structure found with Hi-C (Brooks et al. 2013; Peter et al. 2013; Aschwanden & Peter 2017; Williams et al. 2020). This similarity suggests that (a) the sub-structure is similar for TNE and non-TNE loops (assuming that at least part of the investigated loops by Hi-C are not under TNE), and that (b) this morphology does not directly depend on the spatial scales of the heating in the lower atmosphere. For instance, we know that the latter determines the spatial distribution of the rain showers (Şahin & Antolin 2022), but clearly, the rain showers do not have the same widths as rain clumps (they differ by an order of magnitude). Hence, a different mechanism may cause the fine-scale structure for the rain and the coronal strands. This mechanism may be the same in the case of TNE loops and may correspond to the CCTR produced by thermal instability, as shown in Antolin et al. (2022).

The observed speeds for the coronal rain clumps exhibit a wide projected velocity distribution, as reported in the past (e.g. Antolin & Rouppe van der Voort 2012; Kohutova & Verwichte 2016; Verwichte et al. 2017; Schad 2017). The peak of the observed distribution is below 50 km s^{-1}, with minima and maxima of 10−150 km s^{-1}. This peak contrasts with previously observed peaks of 80−100 km s^{-1} (Antolin 2020). This may be explained by the fact that previous reports focused on off-limb coronal rain for which the FOV is small and only captures a small region around the footpoint (a constraint of current ground-based instrumentation that depends on AO locking). Here, we were able to detect the rain closer to its formation time

higher up along the loop, where the speeds are naturally lower. This agrees with a recent AR-scale study of coronal rain with IRIS by Şahin et al. (2023) and with 2.5D MHD numerical simulations (Li et al. 2022).

Most of the rain events we observed are rooted in moss, with strong jet activity at the footpoints. Previous studies have indicated that strong heating may occur in these regions (Testa et al. 2014; Chitta et al. 2018; Tiwari et al. 2019; Nived et al. 2021), which are favourable for the onset of TNE-TI. In addition, we also observed a structure undergoing a large-scale reconfiguration on April 1st (region 1). This topological change may play a major role in triggering TI due to the expected long-wavelength perturbations (e.g. through magnetic pressure). Through coronal rain tracking, we were able to detect a null-point topology at the footpoint of one of the loops. These structures are preferential locations for magnetic reconnection and therefore heating (Chitta et al. 2017; Priest et al. 2018; Syntelis et al. 2019).

The availability of two co-temporal observations in similar TR lines but with very different LOS, provided by SDO and Solar Orbiter in quadrature, allowed us to disentangle the effect of LOS superposition and spatial resolution to some extent. Large-scale events such as those of March 30 and most of April 1st were not detected in AIA 171, suggesting that LOS superposition is strong. On the other hand, the various events observed on April 1st with $\mathrm{HRI_{EUV}}$ pale in comparison to the spatial extent seen in AIA 304 for that day, as also indicated by the SPICE observations. This suggests that although $\mathrm{HRI_{EUV}}$ is a game changer for observing coronal rain on-disk (in terms of its fine-structure and the associated EUV changes), it is not the ideal channel for detecting how pervasive the phenomenon is in the solar atmosphere. Still, the $\mathrm{HRI_{EUV}}$ observations show for the first time the extent of the EUV variation associated with coronal rain events. We see EUV variation from the small scales of rain clumps and fireballs to the large loop scales of CCTR-induced coronal strands and rebound shocks and flows that partly reheat the loop bundles. This supports previous suggestions based on numerical simulations (Antolin et al. 2022) that the TNE-TI scenario plays a major role in the observed filamentary morphology and high variability of the corona in TR and low coronal spectral lines (Kjeldseth-Moe & Brekke 1998; Ugarte-Urra et al. 2009; Hinode Review Team 2019).

Acknowledgements. Solar Orbiter is a space mission of international collaboration between ESA and NASA, operated by ESA. The EUI instrument was built by CSL, IAS, MPS, MSSL/UCL, PMOD/WRC, ROB, LCF/IO with funding from the Belgian Federal Science Policy Office (BELPSO); Centre National d'Études Spatiales (CNES); the UK Space Agency (UKSA); the Deutsche Zentrum für Luft- und Raumfahrt e.V. (DLR); and the Swiss Space Office (SSO). The building of EUI was the work of more than 150 individuals during more than 10 years. We gratefully acknowledge all the efforts that have led to a successfully operating instrument. The development of SPICE has been funded by ESA member states and ESA. It was built and is operated by a multi-national consortium of research institutes supported by their respective funding agencies: STFC RAL (UKSA, hardware lead), IAS (CNES, operations lead), GSFC (NASA), MPS (DLR), PMOD/WRC (Swiss Space Office), SwRI (NASA), UiO (Norwegian Space Agency). SDO is a mission for NASA's Living With a Star (LWS) program. The ROB co-authors thank the Belgian Federal Science Policy Office (BELSPO) for the provision of financial support in the framework of the PRODEX Programme of the European Space Agency (ESA) under contract numbers 4000112292, 4000134088, 4000134474, and 4000136424. P.A. and D.M.L. acknowledge funding from STFC Ernest Rutherford Fellowships No. ST/R004285/2 and ST/R003246/1, respectively. A.D. acknowledges the funding by CNES and EDOM. S.P. acknowledges the funding by CNES through the MEDOC data and operations center. L.P.C. gratefully acknowledges funding by the European Union (ERC, ORIGIN, 101039844). Views and opinions expressed are however those of the author(s) only and do not necessarily reflect those of the European Union or the European Research Council. Neither the European Union nor the granting authority can be held responsible for them. This research was supported by the International Space Science Institute (ISSI) in Bern, through ISSI International Team project #545 ('Observe Local Think Global: What Solar Observations can Teach us about Multiphase Plasmas across Physical Scales').

References

Ahn, K., Chae, J., Cho, K.-S., et al. 2014, Sol. Phys., 289, 4117
Antiochos, S. K., & Klimchuk, J. A. 1991, ApJ, 378, 372
Antiochos, S. K., MacNeice, P. J., Spicer, D. S., & Klimchuk, J. A. 1999, ApJ, 512, 985
Antolin, P. 2020, Plasma Phys. Control. Fusion, 62, 014016
Antolin, P., & Froment, C. 2022, Front. Astron. Space Sci., 9, 820116
Antolin, P., & Rouppe van der Voort, L. 2012, ApJ, 745, 152
Antolin, P., & Shibata, K. 2010, ApJ, 712, 494
Antolin, P., Shibata, K., & Vissers, G. 2010, ApJ, 716, 154
Antolin, P., Vissers, G., Pereira, T. M. D., Rouppe van der Voort, L., & Scullion, E. 2015, ApJ, 806, 81
Antolin, P., Martínez-Sykora, J., & Şahin, S. 2022, ApJ, 926, L29
Anzer, U., & Heinzel, P. 2005, ApJ, 622, 714
Aschwanden, M. J., & Peter, H. 2017, ApJ, 840, 4
Aschwanden, M. J., Schrijver, C. J., & Alexander, D. 2001, ApJ, 550, 1036
Auchère, F., Bocchialini, K., Solomon, J., & Tison, E. 2014, A&A, 563, A8
Auchère, F., Froment, C., Soubrié, E., et al. 2018, ApJ, 853, 176
Auchère, F., Soubrié, E., Pelouze, G., & Buchlin, É. 2023, A&A, 670, A66 (SO Nominal Mission Phase SI)
Beckers, J. M. 1964, Ph.D. Thesis, Sacramento Peak Observatory, Air Force Cambridge Research Laboratories, Mass., USA
Berghmans, D., Auchère, F., Long, D. M., et al. 2021, A&A, 656, L4
Berghmans, D., Antolin, P., Auchère, F., et al. 2023, A&A, 675, A110 (SO Nominal Mission Phase SI)
Brooks, D. H., Warren, H. P., Ugarte-Urra, I., & Winebarger, A. R. 2013, ApJ, 772, L19
Cavagnolo, K. W., Donahue, M., Voit, G. M., & Sun, M. 2008, ApJ, 683, L107
Chen, Y., Przybylski, D., Peter, H., et al. 2021, A&A, 656, L7
Chen, H., Tian, H., Li, L., et al. 2022, A&A, 659, A107
Chitta, L. P., Peter, H., & Young, P. R. 2016, A&A, 587, A20
Chitta, L. P., Peter, H., Solanki, S. K., et al. 2017, ApJS, 229, 4
Chitta, L. P., Peter, H., & Solanki, S. K. 2018, A&A, 615, L9
Chitta, L. P., Peter, H., Parenti, S., et al. 2022, A&A, 667, A166 (SO Nominal Mission Phase SI)
Claes, N., & Keppens, R. 2019, A&A, 624, A96
Claes, N., & Keppens, R. 2021, Sol. Phys., 296, 143
Claes, N., Keppens, R., & Xia, C. 2020, A&A, 636, A112
De Groof, A., Berghmans, D., van Driel-Gesztelyi, L., & Poedts, S. 2004, A&A, 415, 1141
De Groof, A., Bastiaensen, C., Müller, D. A. N., Berghmans, D., & Poedts, S. 2005, A&A, 443, 319
De Pontieu, B., Title, A. M., Lemen, J. R., et al. 2014, Sol. Phys., 289, 2733
De Pontieu, B., Polito, V., Hansteen, V., et al. 2021, Sol. Phys., 296, 84
Fang, X., Xia, C., Keppens, R., & Van Doorsselaere, T. 2015, ApJ, 807, 142
Field, G. B. 1965, ApJ, 142, 531
Foukal, P. 1978, ApJ, 223, 1046
Froment, C., Auchère, F., Bocchialini, K., et al. 2015, ApJ, 807, 158
Froment, C., Auchère, F., Mikić, Z., et al. 2018, ApJ, 855, 52
Froment, C., Antolin, P., Henriques, V. M. J., Kohutova, P., & Rouppe van der Voort, L. H. M. 2020, A&A, 633, A11
Goode, P. R., Denker, C. J., Didkovsky, L. I., Kuhn, J. R., & Wang, H. 2003, J. Korean Astron. Soc., 36, S125
Habbal, S. R., Ronan, R., & Withbroe, G. L. 1985, Sol. Phys., 98, 323
Hinode Review Team (Al-Janabi, K., et al.) 2019, PASJ, 71, R1
Jing, J., Xu, Y., Cao, W., et al. 2016, Sci. Rep., 6, 24319
Johnston, C. D., Cargill, P. J., Antolin, P., et al. 2019, A&A, 625, A149
Kamio, S., Peter, H., Curdt, W., & Solanki, S. K. 2011, A&A, 532, A96
Karpen, J. T., Antiochos, S. K., Hohensee, M., Klimchuk, J. A., & MacNeice, P. J. 2001, ApJ, 553, L85
Kawaguchi, I. 1970, PASJ, 22, 405
Kjeldseth-Moe, O., & Brekke, P. 1998, Sol. Phys., 182, 73
Klimchuk, J. A. 2015, Philos. Trans. R. Soc. London Ser. A, 373, 20140256
Klimchuk, J. A. 2019, Sol. Phys., 294, 173
Klimchuk, J. A., & Luna, M. 2019, ApJ, 884, 68
Kobayashi, K., Cirtain, J., Winebarger, A. R., et al. 2014, Sol. Phys., 289, 4393
Kohutova, P., & Verwichte, E. 2016, ApJ, 827, 39
Kosugi, T., Matsuzaki, K., Sakao, T., et al. 2007, Sol. Phys., 243, 3
Kuin, N. P. M., & Martens, P. C. H. 1982, A&A, 108, L1
Lemen, J. R., Title, A. M., Akin, D. J., et al. 2012, Sol. Phys., 275, 17
Leroy, J. 1972, Sol. Phys., 25, 413
Li, L., Zhang, J., Peter, H., et al. 2018, ApJ, 864, L4

Li, L., Peter, H., Chitta, L. P., et al. 2019, ApJ, 884, 34
Li, X., Keppens, R., & Zhou, Y. 2022, ApJ, 926, 216
Lionello, R., Alexander, C. E., Winebarger, A. R., Linker, J. A., & Mikić, Z. 2016, ApJ, 818, 129
Lipschultz, B. 1987, J. Nucl. Mater., 145–147, 15
Luna, M., Karpen, J. T., & DeVore, C. R. 2012, ApJ, 746, 30
Malanushenko, A., Cheung, M. C. M., DeForest, C. E., Klimchuk, J. A., & Rempel, M. 2022, ApJ, 927, 1
Mampaey, B., Verbeeck, F., Stegen, K., et al. 2022, SolO/EUI Data Release 5.0 2022-04 (Royal Observatory of Belgium (ROB)), https://doi.org/10.24414/2qfw-tr95
Mandal, S., Peter, H., Chitta, L. P., et al. 2023, A&A, 670, L3 (SO Nominal Mission Phase SI)
Martínez-Sykora, J., De Pontieu, B., De Moortel, I., Hansteen, V. H., & Carlsson, M. 2018, ApJ, 860, 116
Mason, E. I., Antiochos, S. K., & Viall, N. M. 2019, ApJ, 874, L33
Mendoza-Briceño, C. A., Erdélyi, R., & Sigalotti, L. D. G. 2002, ApJ, 579, L49
Mendoza-Briceño, C. A., Sigalotti, L. D. G., & Erdélyi, R. 2005, ApJ, 624, 1080
Mikić, Z., Lionello, R., Mok, Y., Linker, J. A., & Winebarger, A. R. 2013, ApJ, 773, 94
Mok, Y., Drake, J. F., Schnack, D. D., & van Hoven, G. 1990, ApJ, 359, 228
Müller, D. A. N., Hansteen, V. H., & Peter, H. 2003, A&A, 411, 605
Müller, D. A. N., Fleck, B., Dimitoglou, G., et al. 2009, Comput. Sci. Eng., 11, 38
Müller, D., St. Cyr, O. C., Zouganelis, I., et al. 2020, A&A, 642, A1
Nived, V. N., Scullion, E., Doyle, J. G., et al. 2021, MNRAS, 509, 5523
Parker, E. N. 1953, ApJ, 117, 431
Pelouze, G., Auchère, F., Bocchialini, K., et al. 2022, A&A, 658, A71
Pesnell, W. D., Thompson, B. J., & Chamberlin, P. C. 2012, Sol. Phys., 275, 3
Peter, H., Bingert, S., & Kamio, S. 2012, A&A, 537, A152
Peter, H., Bingert, S., Klimchuk, J. A., et al. 2013, A&A, 556, A104
Priest, E. R., Chitta, L. P., & Syntelis, P. 2018, ApJ, 862, L24
Rachmeler, L. A., Winebarger, A. R., Savage, S. L., et al. 2019, Sol. Phys., 294, 174
Reale, F. 2010, Liv. Rev. Sol. Phys., 7, 5
Reale, F., Peres, G., & Serio, S. 1996, A&A, 316, 215
Reep, J. W., Antolin, P., & Bradshaw, S. J. 2020, ApJ, 890, 100
Rochus, P., Auchère, F., Berghmans, D., et al. 2020, A&A, 642, A8
Rosner, R., Tucker, W. H., & Vaiana, G. S. 1978, ApJ, 220, 643
Şahin, S., & Antolin, P. 2022, ApJ, 931, L27
Şahin, S., Antolin, P., Froment, C., & Schad, T. A. 2023, ApJ, 950, 171
Schad, T. 2017, Sol. Phys., 292, 132
Scharmer, G. B., Bjelksjo, K., Korhonen, T. K., Lindberg, B., & Petterson, B. 2003, SPIE Conf. Ser., 4853, 341
Schrijver, C. J. 2001, Sol. Phys., 198, 325
Sharma, P. 2013, Astron. Soc. India Conf. Ser., 9, 27
SPICE Consortium (Anderson, M., et al.) 2020, A&A, 642, A14
Stacey, W. M. 1996, Phys. Plasmas, 3, 2673
Susino, R., Lanzafame, A. C., Lanza, A. F., & Spadaro, D. 2010, ApJ, 709, 499
Syntelis, P., Priest, E. R., & Chitta, L. P. 2019, ApJ, 872, 32
Testa, P., De Pontieu, B., Allred, J., et al. 2014, Science, 346, 1255724
Tiwari, S. K., Panesar, N. K., Moore, R. L., et al. 2019, ApJ, 887, 56
Ugarte-Urra, I., Warren, H. P., & Brooks, D. H. 2009, ApJ, 695, 642
Van Doorsselaere, T., Gijsen, S. E., Andries, J., & Verth, G. 2014, ApJ, 795, 18
Van Doorsselaere, T., Srivastava, A. K., Antolin, P., et al. 2020, Space Sci. Rev., 216, 140
Vashalomidze, Z., Kukhianidze, V., Zaqarashvili, T. V., et al. 2015, A&A, 577, A136
Verwichte, E., Antolin, P., Rowlands, G., Kohutova, P., & Neukirch, T. 2017, A&A, 598, A57
Vial, J. C., & Engvold, O. 2015, Astrophys. Space Sci. Lib., 415, 1
Viall, N. M., & Klimchuk, J. A. 2012, ApJ, 753, 35
Viall, N., De Moortel, I., & Downs, C. 2021, The Heating of the Solar Corona (American Geophysical Union (AGU)), 35
Vissers, G., & Rouppe van der Voort, L. 2012, ApJ, 750, 22
Waters, T., & Proga, D. 2019, ApJ, 875, 158
White, S. D. M., & Rees, M. J. 1978, MNRAS, 183, 341
Wiik, J. E., Schmieder, B., Heinzel, P., & Roudier, T. 1996, Sol. Phys., 166, 89
Williams, T., Walsh, R. W., Winebarger, A. R., et al. 2020, ApJ, 892, 134
Winebarger, A. R., Lionello, R., Downs, C., Mikić, Z., & Linker, J. 2018, ApJ, 865, 111
Zouganelis, I., De Groof, A., Walsh, A. P., et al. 2020, A&A, 642, A3

[1] Department of Mathematics, Physics and Electrical Engineering, Northumbria University, Newcastle upon Tyne NE1 8ST, UK
e-mail: patrick.antolin@northumbria.ac.uk
[2] Université Paris-Saclay, CNRS, Institut d'Astrophysique Spatiale, 91405 Orsay, France
[3] Max Planck Institute for Solar System Research, Justus-von-Liebig-Weg 3, 37077 Göttingen, Germany
[4] Solar-Terrestrial Centre of Excellence, SIDC, Royal Observatory of Belgium, Ringlaan 3 Av. Circulaire, 1180 Brussels, Belgium
[5] Physikalisch-Meteorologisches Observatorium Davos, World Radiation Center, 7260 Davos Dorf, Switzerland
[6] ETH Zürich, Institute for Particle Physics and Astrophysics, Wolfgang-Pauli-Strasse 27, 8093 Zürich, Switzerland
[7] European Space Agency, ESTEC, Keplerlaan 1, PO Box 299, 2200 AG Noordwijk, The Netherlands
[8] UCL-Mullard Space Science Laboratory, Holmbury St. Mary, Dorking, Surrey RH5 6NT, UK
[9] Southwest Research Institute, 1050 Walnut Street, Suite 300, Boulder, CO 80302, USA
[10] Skobeltsyn Institute of Nuclear Physics, Moscow State University, 119992 Moscow, Russia
[11] Sorbonne Université, Observatoire de Paris – PSL, École Polytechnique, Institut Polytechnique de Paris, CNRS, Laboratoire de Physique des Plasmas (LPP), 4 Place Jussieu, 75005 Paris, France
[12] Rosseland Centre for Solar Physics, University of Oslo, PO Box 1029, Blindern 0315, Oslo, Norway
[13] Laboratoire Charles Fabry, Institut d'Optique Graduate School, Université Paris-Saclay, 91127 Palaiseau Cedex, France
[14] Centre Spatial de Liège, Université de Liège, Av. du Pré-Aily B29, 4031 Angleur, Belgium
[15] AESTER COGNITIO, 27 Rue de Naples, 75008 Paris, France
[16] LATMOS, CNRS, UVSQ, Sorbonne Université, 78280 Guyancourt, France
[17] Centre for mathematical Plasma Astrophysics, Department of Mathematics, KU Leuven, Celestijnenlaan 200B bus 2400, 3001 Leuven, Belgium
[18] Institute of Physics, University of Maria Curie-Skłodowska, Pl. M. Curie-Skłodowskiej 5, 20-031 Lublin, Poland
[19] Astrophysics Research Centre, School of Mathematics and Physics, Queen's University Belfast, University Road, Belfast BT7 1NN, Northern Ireland, UK

Appendix A: Multi-wavelength views with SPICE on March 30 and April 1st

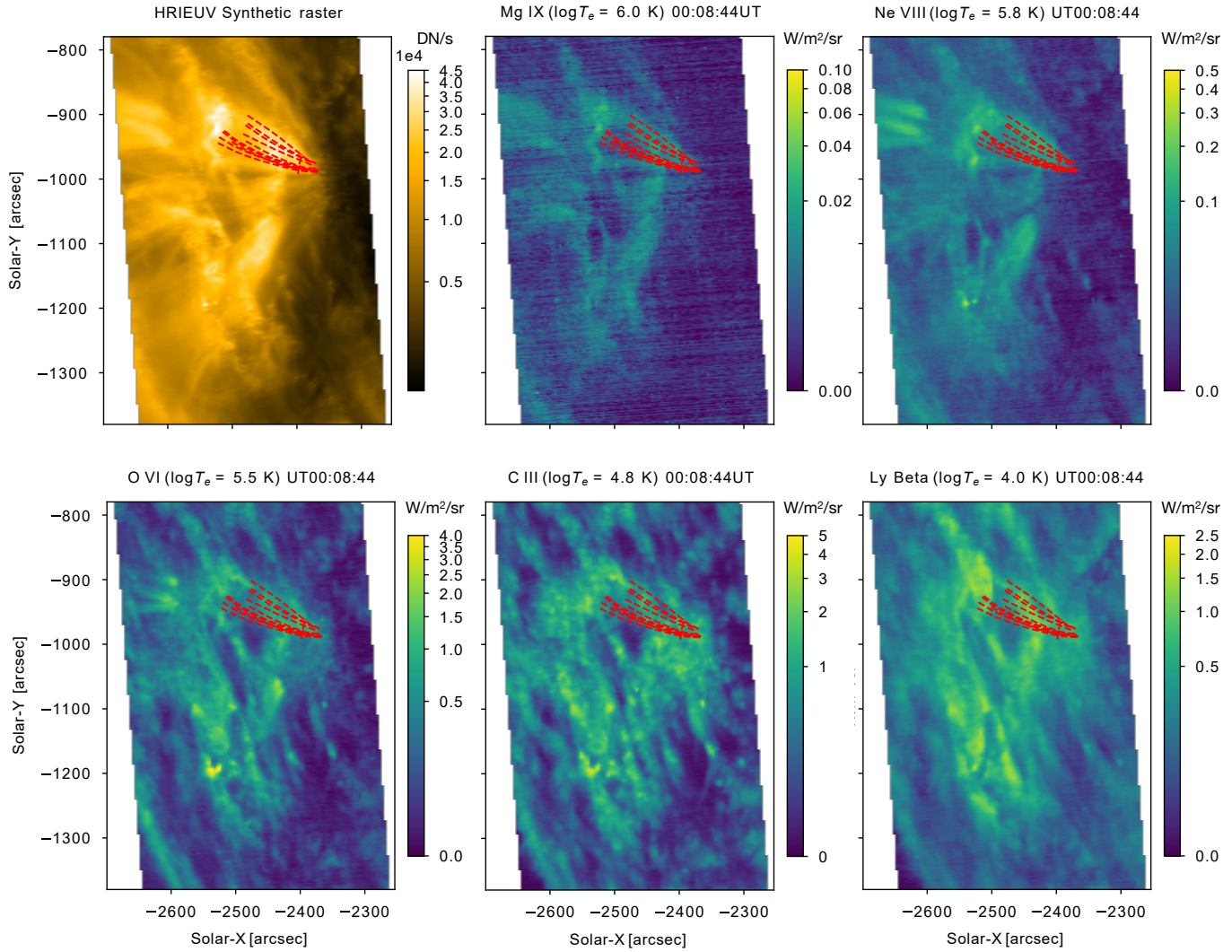

Fig. A.1. SPICE multi-wavelength full FOV on March 30. The SPICE FOV is the same as shown in Figure 2 (top). The HRI_{EUV} panel corresponds to a synthetic raster matching the time of the SPICE raster (see the text for details) including spatial binning to match the SPICE plate scale. Each SPICE panel shows the total intensity over the indicated spectral line, together with its temperature of maximum formation. The overlaid red curves denote the rain paths seen with HRI_{EUV} (see Figure 5).

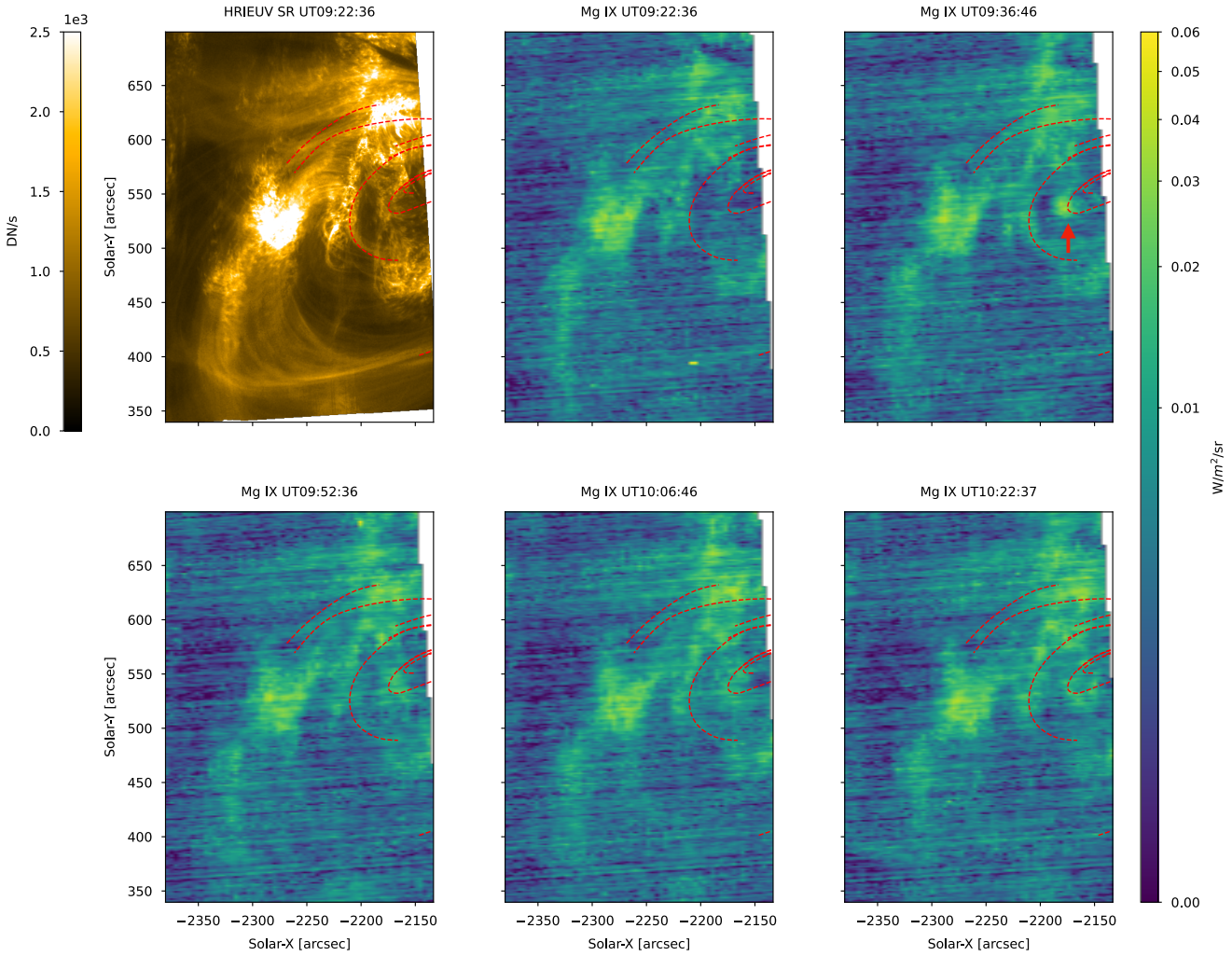

Fig. A.2. Same as in Figure 12, but for the Mg IX line.

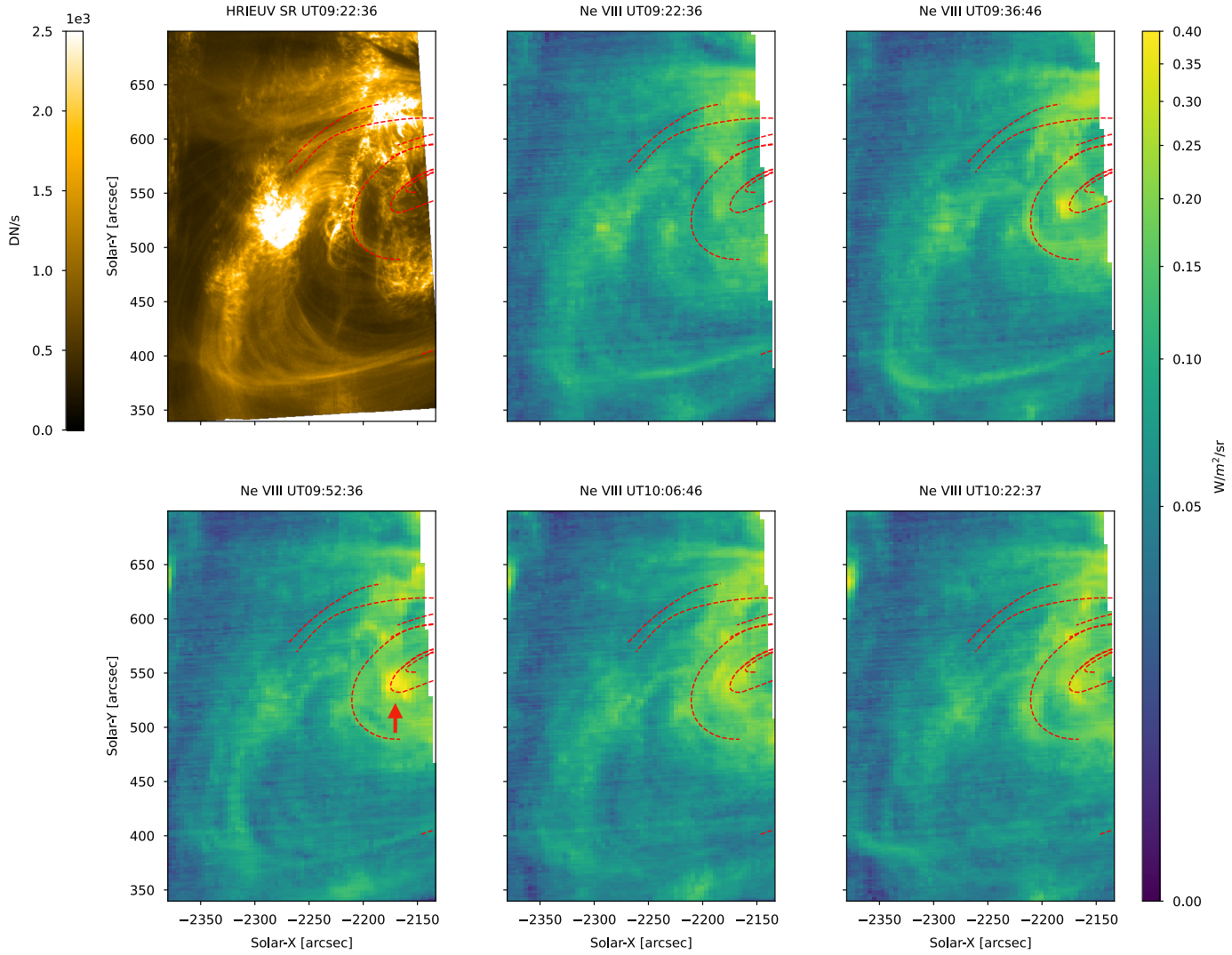

Fig. A.3. Same as in Figure 12, but for the Ne VIII line.

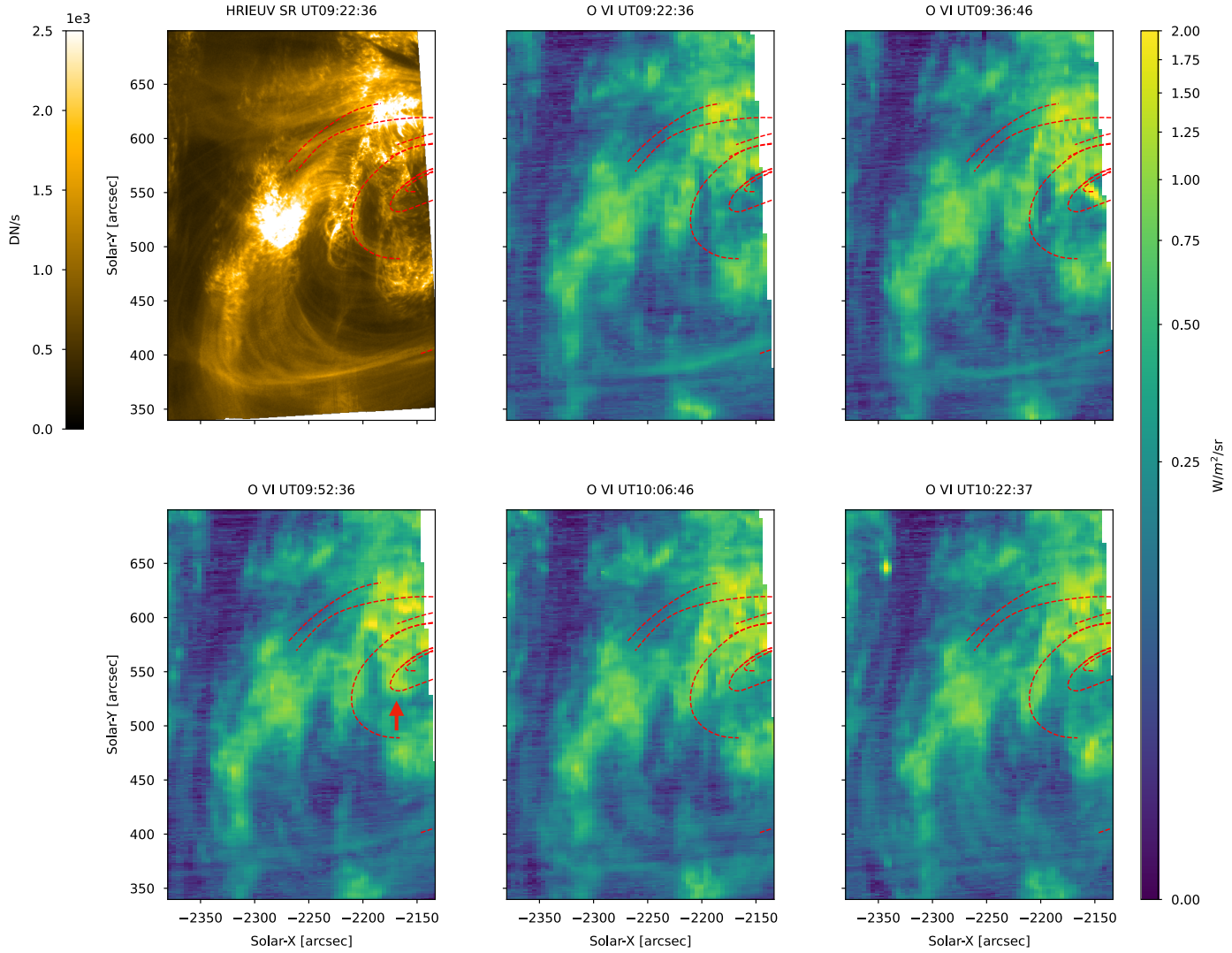

Fig. A.4. Same as in Figure 12, but for the O VI line.

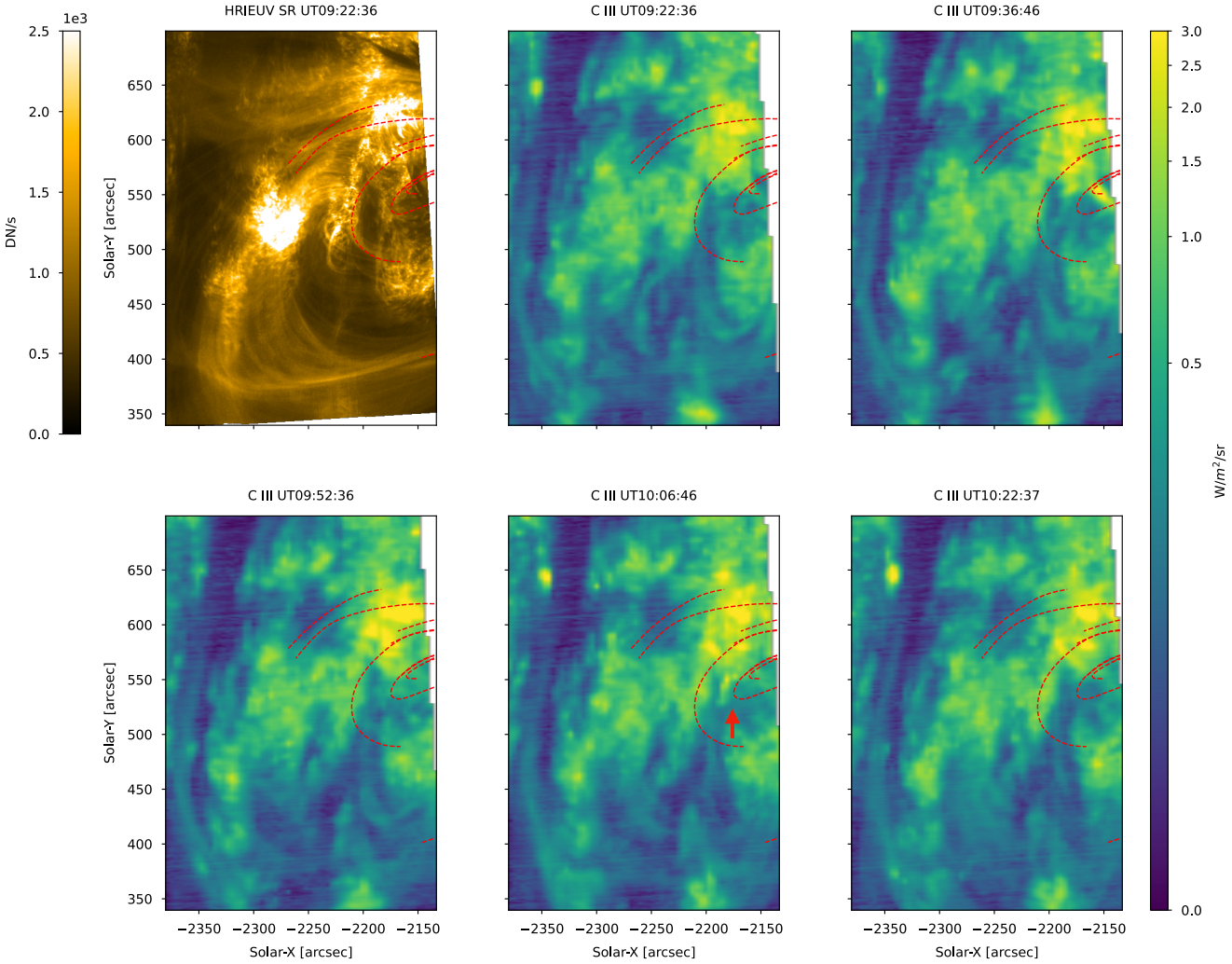

Fig. A.5. Same as in Figure 12, but for the C III line.

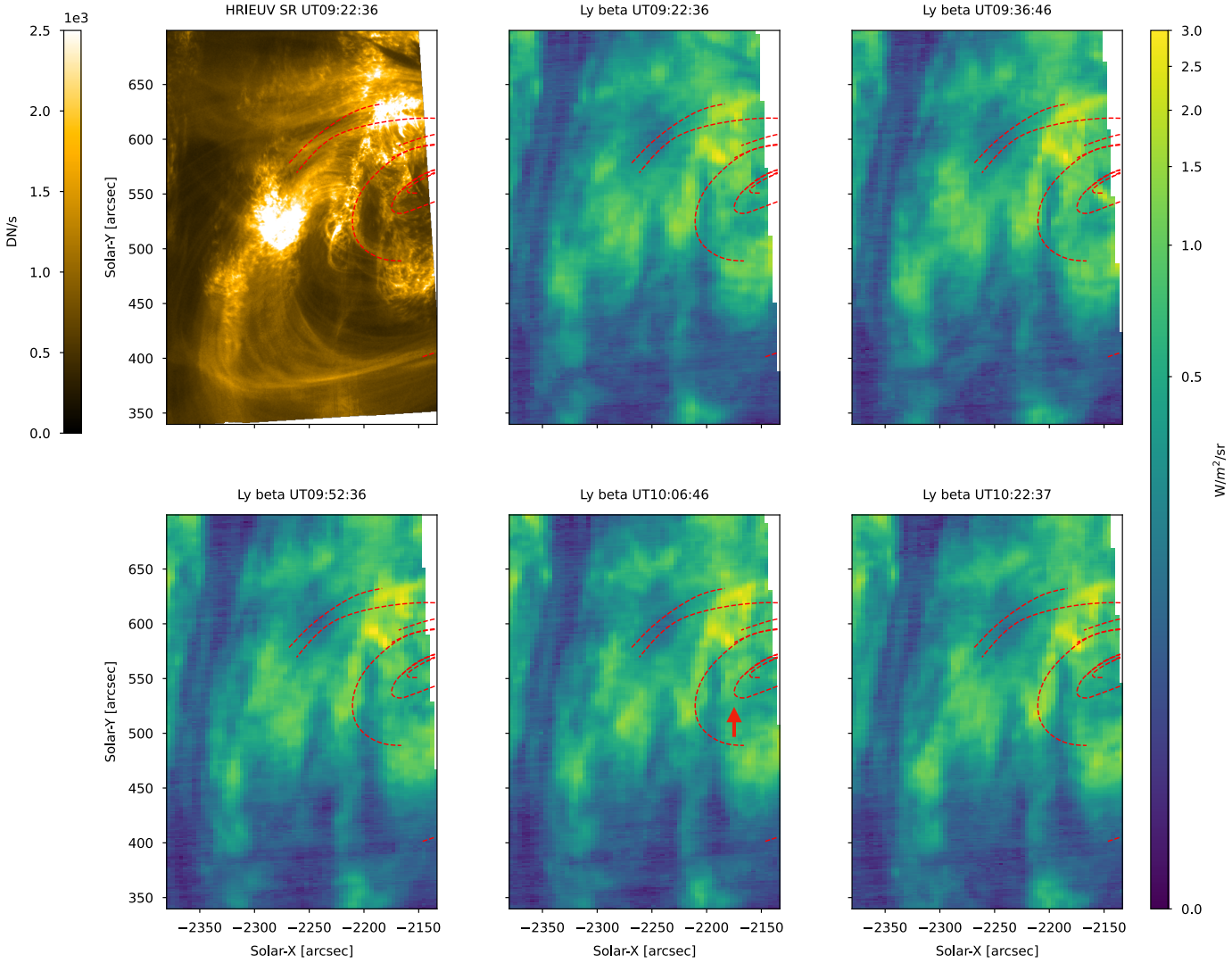

Fig. A.6. Same as in Figure 12, but for the Lyman-β line.

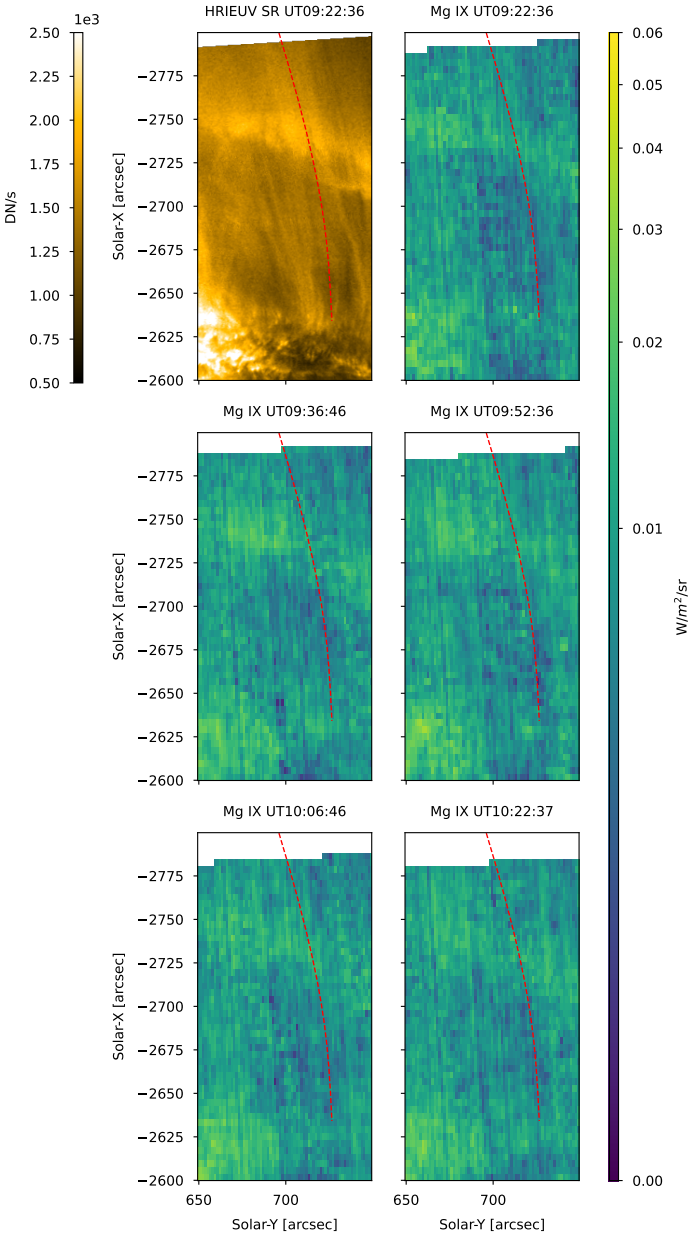

Fig. A.7. Same as in Figure 17, but for the Mg IX line.

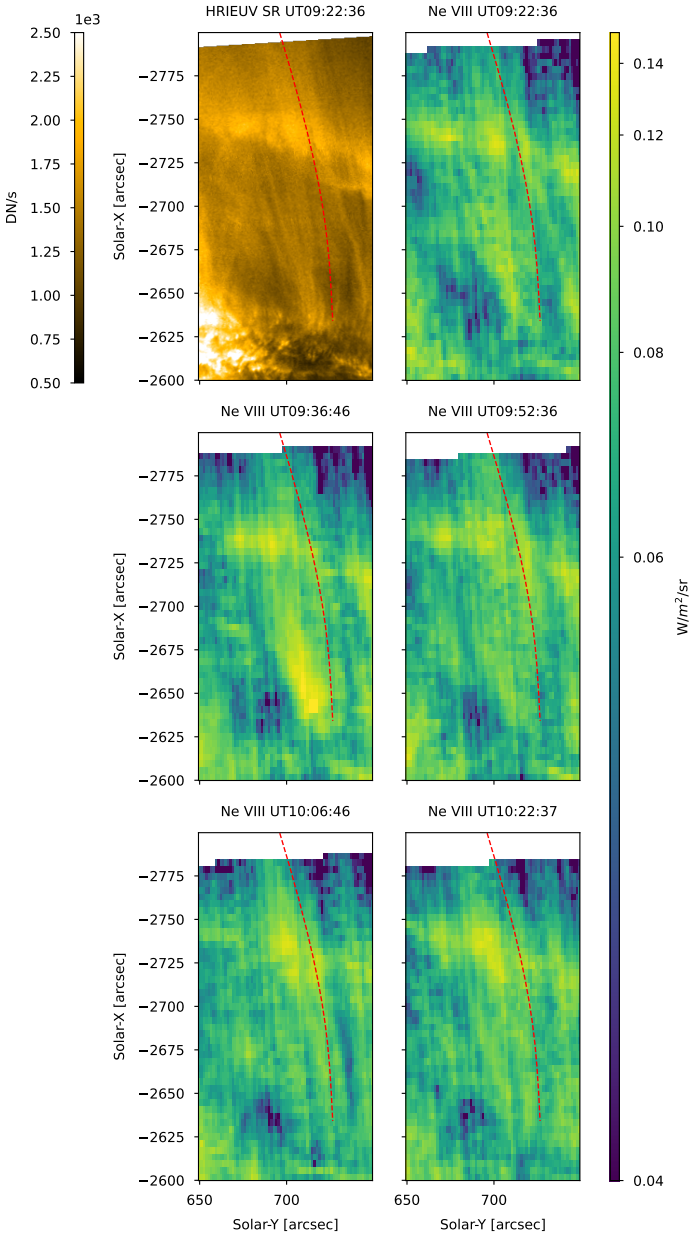

Fig. A.8. Same as in Figure 17, but for the Ne VIII line.

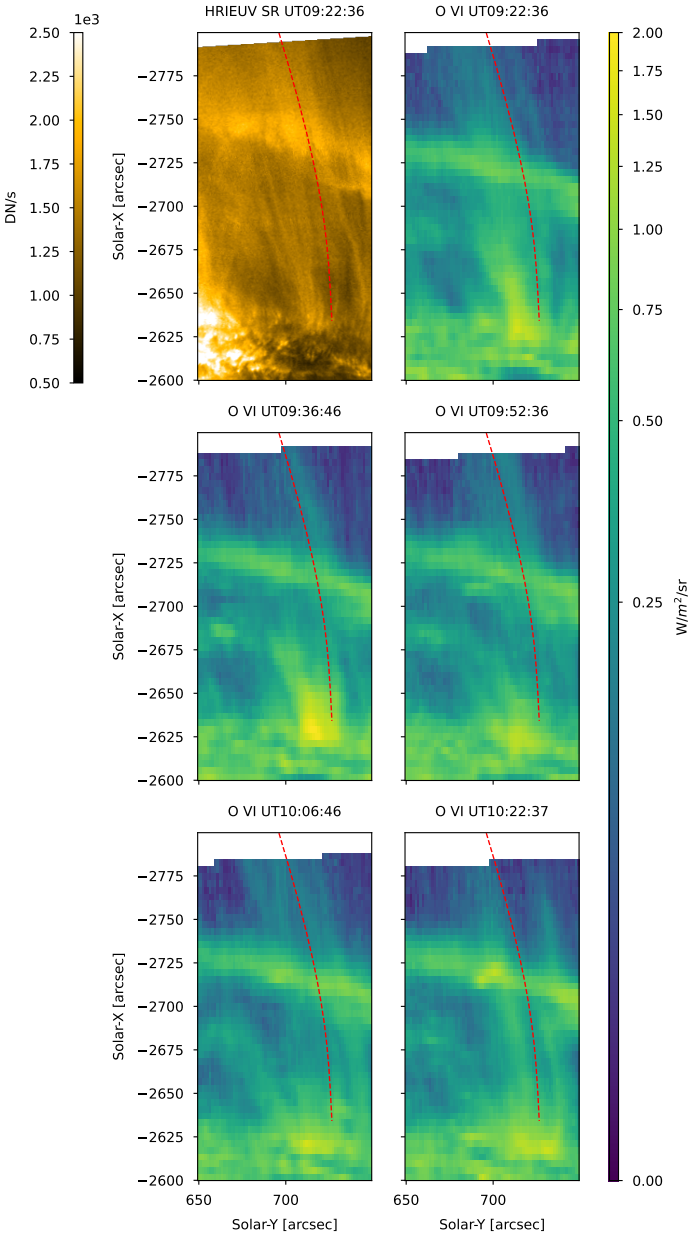

Fig. A.9. Same as in Figure 17, but for the O VI line.

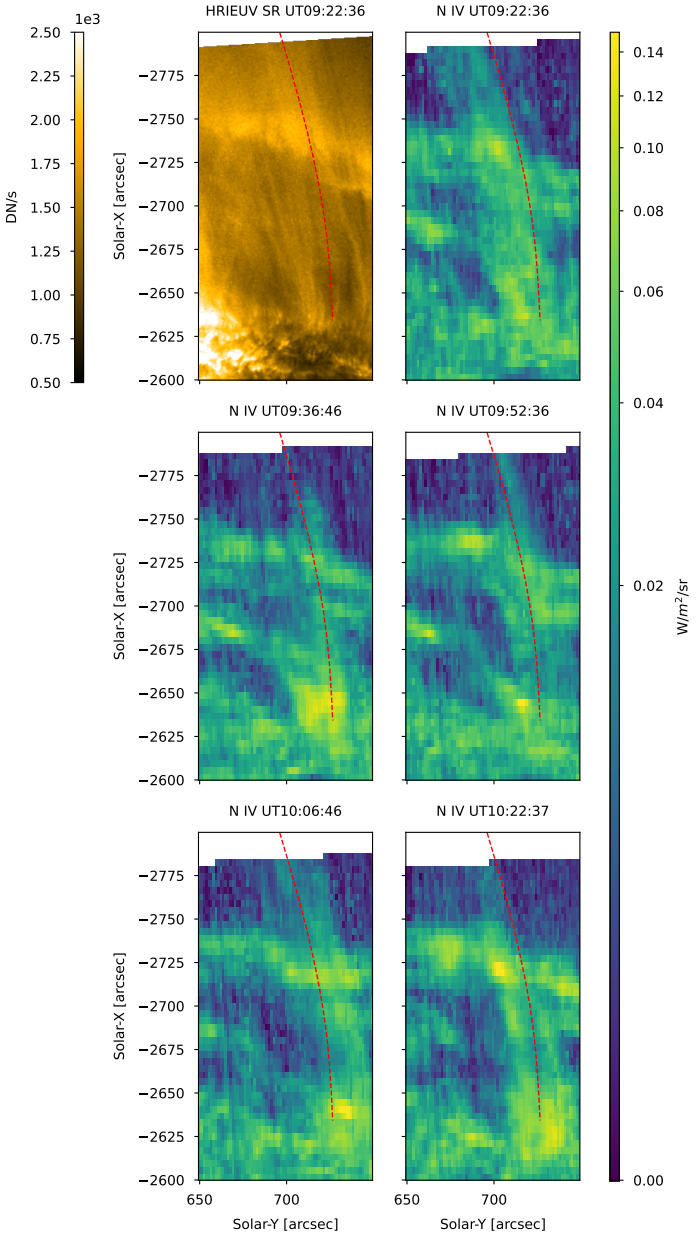

Fig. A.10. Same as in Figure 17, but for the N IV line.

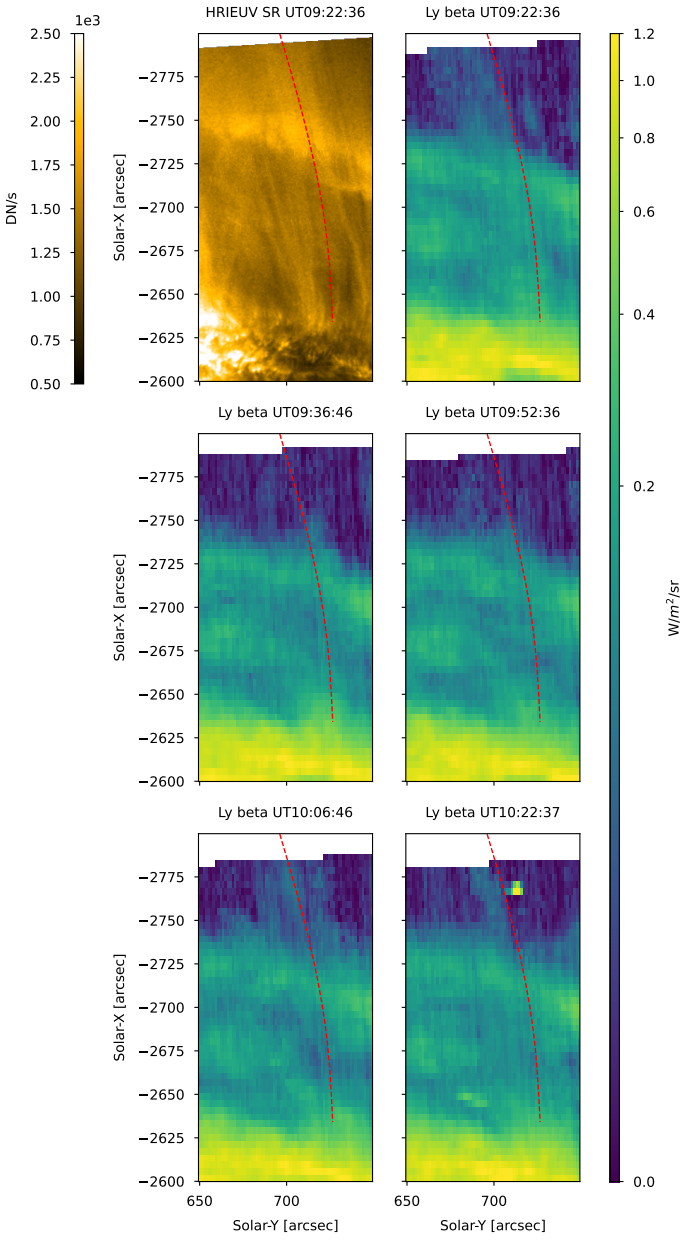

Fig. A.11. Same as in Figure 17, but for the Lyman-β line.

Appendix B: Time-distance diagrams with HRI$_{EUV}$ on April 1st

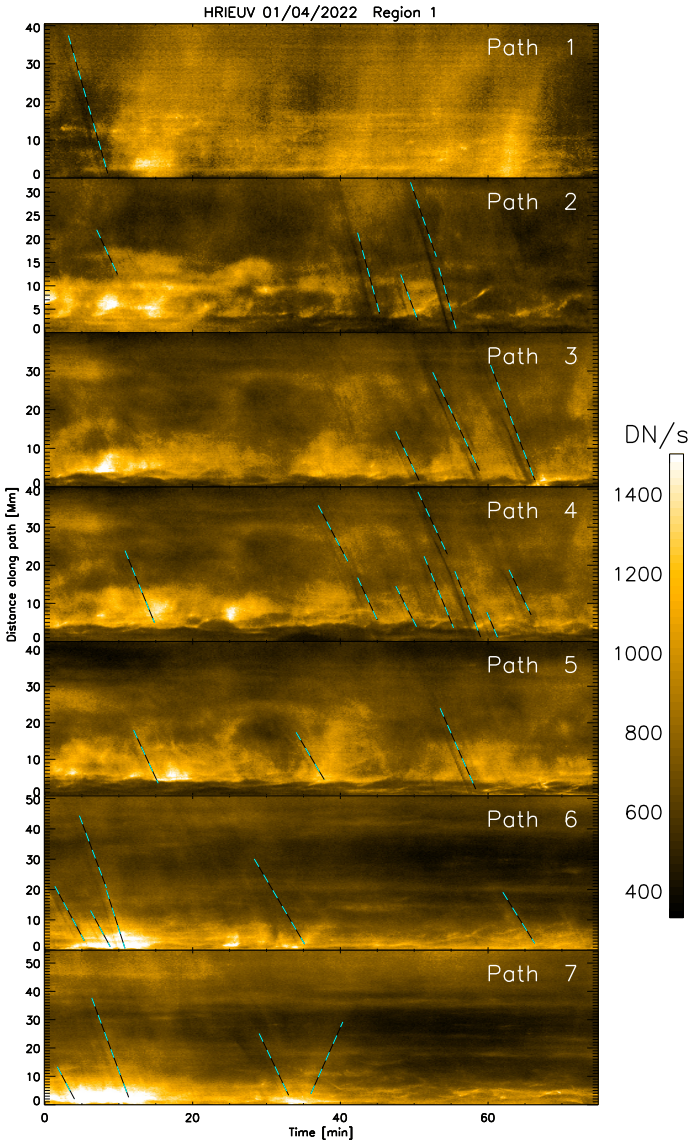

Fig. B.1. Time-distance diagram for the rain paths tracked in region 1 shown in Figure 10. The dashed cyan-black lines with negative slopes track the dark or bright absorption or emission features produced by several rain clumps falling into the chromosphere. A few bright upward-propagating features can also be seen (positive slopes). Zero distance corresponds to the footpoint of the loop (top right panel of Figure 10).

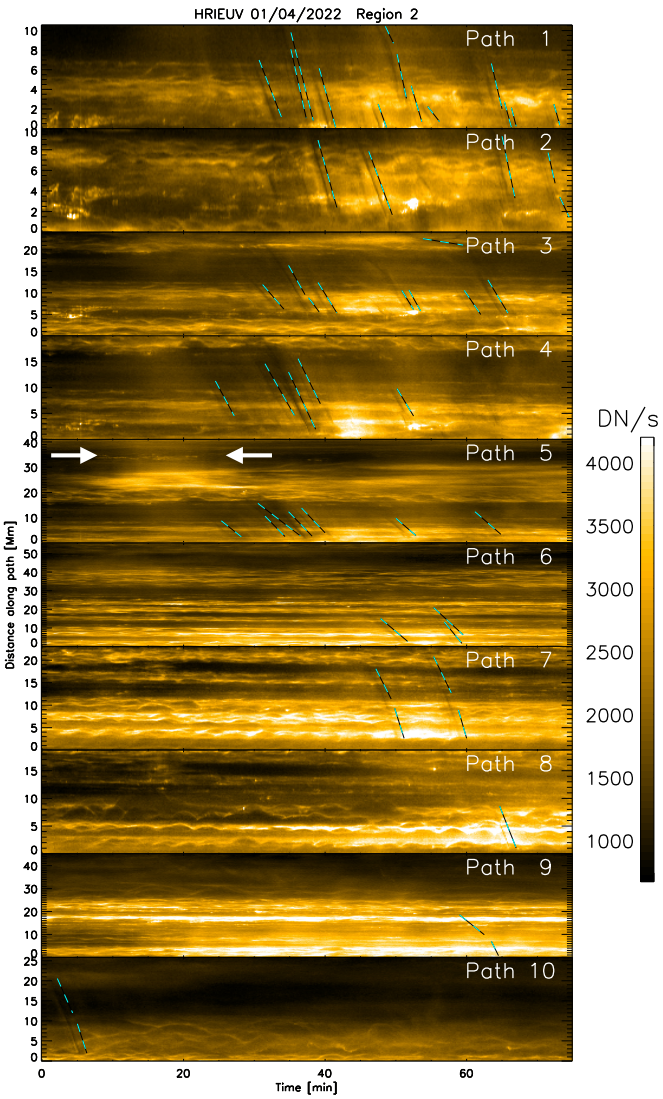

Fig. B.2. Time-distance diagrams for the paths of the rain clumps shown in Figure 11. The dashed cyan-black lines correspond to coronal rain tracks along the paths, with zero distance corresponding to the loop footpoints on the right side in Figure 11. The lines are offset in time by 1 min to show the rain features better. The white arrows in the time-distance diagrams for path 5 indicate the times when the loop brightens prior to the appearance of the rain.

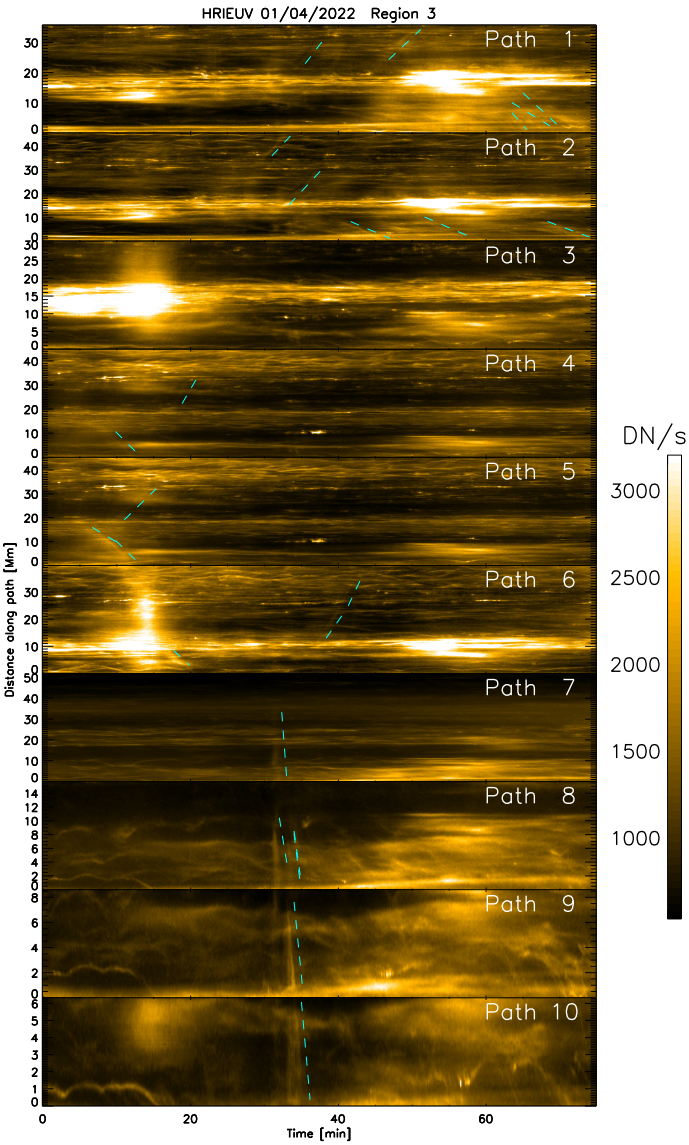

Fig. B.3. Time-distance diagrams for the paths of the rain clumps shown in Figure 13. The dashed cyan lines correspond to coronal rain tracks along the paths, with zero distance corresponding to the loop footpoints (left in Figure 13). The lines are offset in time by 1 min to show the rain features better. The loop brightening is seen clearly in paths 3 and 6 at time $t = 15$ min.